creative commons
COMMONS DEED

저작자표시-비영리-변경금지 2.0 대한민국

이용자는 아래의 조건을 따르는 경우에 한하여 자유롭게

- 이 저작물을 복제, 배포, 전송, 전시, 공연 및 방송할 수 있습니다.

다음과 같은 조건을 따라야 합니다:

저작자표시. 귀하는 원저작자를 표시하여야 합니다.

비영리. 귀하는 이 저작물을 영리 목적으로 이용할 수 없습니다.

변경금지. 귀하는 이 저작물을 개작, 변형 또는 가공할 수 없습니다.

- 귀하는, 이 저작물의 재이용이나 배포의 경우, 이 저작물에 적용된 이용허락조건을 명확하게 나타내어야 합니다.
- 저작권자로부터 별도의 허가를 받으면 이러한 조건들은 적용되지 않습니다.

저작권법에 따른 이용자의 권리는 위의 내용에 의하여 영향을 받지 않습니다.

이것은 이용허락규약(Legal Code)을 이해하기 쉽게 요약한 것입니다.

Disclaimer

dCollection

[UCI]I804:31001-200000108305

ULSAN NATIONAL INSTITUTE OF SCIENCE AND TECHNOLOGY

Master's Thesis

MULTI-SPECIES MULTI-PHYSICS MODELING AND VALIDATION OF HYDRODYNAMIC ELECTROCHEMICAL SYSTEM FOR USED NUCLEAR FUEL

Dokyu Kang

Department of Nuclear Engineering

Graduate School of UNIST

2018

ULSAN NATIONAL INSTITUTE OF
SCIENCE AND TECHNOLOGY

Multi-species Multi-physics Modeling and Validation of Hydrodynamic Electrochemical System for Used Nuclear Fuel

Dokyu Kang

Department of Nuclear Engineering

Graduate School of UNIST

ULSAN NATIONAL INSTITUTE OF
SCIENCE AND TECHNOLOGY

Multi-species Multi-physics Modeling and Validation of Hydrodynamic Electrochemical System for Used Nuclear Fuel

A thesis
submitted to the Graduate School of UNIST
in partial fulfillment of the
requirements for the degree of
Master of Science

Dokyu Kang

July 5, 2018
Approved by

_____

Advisor
Hee Reyoung Kim

ULSAN NATIONAL INSTITUTE OF
SCIENCE AND TECHNOLOGY

Multi-species Multi-physics Modeling and Validation of Hydrodynamic Electrochemical System for Used Nuclear Fuel

Dokyu Kang

This certifies that the thesis of Dokyu Kang is approved.

July 5, 2018

_____

Advisor: Hee Reyoung Kim

_____

Sungyeol Choi: Thesis Committee Member #1

_____

Jaeyeong Park: Thesis Committee Member #2

ULSAN NATIONAL INSTITUTE OF
SCIENCE AND TECHNOLOGY

Abstract

Accurate predictions of processes in hydrodynamic electrochemical systems require an understanding of both the surface electrochemical reactions and the bulk mass transport. Complete coupling of electrochemistry and fluid mechanics is computationally very rich for multidimensional modeling since it involves multiple components across multi-phases at the same time. Therefore, this study develops a computational model that combines a 3D model for calculating single-species mass transport and a 2D model for calculating multi-species electrochemical reactions. The computational model is validated against lab-scale experimental data using a rotating cylinder solid metal cathode and liquid metal anode in the Argonne National Laboratory. The 3D model assumes that U, the representative component in the system, dominates the hydrodynamic behavior, and thus calculates mass transport caused by the rotating solid cylinder electrode. The 2D model still reflects the diffusion of U, Pu, and Nd within a diffusion boundary layer and the bulk concentration changes of these components. The 3D model provides a diffusion layer thickness reflecting convective mass transfer effects to the 2D model. The results of the proposed model show good agreement with the reference experiment, and the model can be considered an important tool for investigating the multidimensional distributions of hydrodynamic and electrochemical variables.

ULSAN NATIONAL INSTITUTE OF
SCIENCE AND TECHNOLOGY

CONTENTS

ULSAN NATIONAL INSTITUTE OF
SCIENCE AND TECHNOLOGY

LIST OF FIGURES

ULSAN NATIONAL INSTITUTE OF SCIENCE AND TECHNOLOGY

ULSAN NATIONAL INSTITUTE OF
SCIENCE AND TECHNOLOGY

LIST OF TABLES

ULSAN NATIONAL INSTITUTE OF
SCIENCE AND TECHNOLOGY

I. Introduction

1.1 Background

Nuclear energy has provided a clean source of electricity without carbon dioxide emission, since the first operation of nuclear power plant (NPP), Kori Unit 1 at 1978 in South Korea. Now South Korea has 24 nuclear power plants in operation and the first NPP, Kori Unit 1 has been shut down recently. South Korea now has been facing decommission phase of NPP after the development phase. However, 485 bundles of used nuclear fuels has been stored in the water pool inside the Kori Unit 1 and these used nuclear fuel have to be moved to a disposal site for the decommissioning work. In addition, large amount of used nuclear fuels have been accumulated in the water pool inside not only the Kori Unit 1 but also other nuclear power plants in South Korea through several decades of NPP operation.

Table 1 shows the inventories of used nuclear fuel in the NPP of the South Korea. Although high density storage racks were installed at Kori Units 3&4, Hanul Units 1~4 and Hanbit Units 1,3,4,5, and 6 in order to expand the spent fuel storage capacity, the inventories of the most of sites are approaching the limitation of storage capacity [1].

After the on-site storage of used nuclear fuels at the water pool, the radiation and decay heat are significantly reduced and they have to be moved to dry interim storage for further reduction of radioactivity and heat by radioactive decay and natural cooling for 50~100 years. At last, they will be disposed in deep geological repository and isolated from humanity.

Used nuclear fuel consists of U, TRUs, long-lived fission products, and short-lived fission products as shown in **Figure 1**. (a). Their effect to the geological repository are different based on their decay and chemical characteristic. The thermal-power profiles of spent LWR fuel and its various contributors were shown in the **Figure 2**. Up to several decades of discharge, the most of thermal power of spent fuel comes from the short-lived radionuclides (^{90}Sr and ^{137}Cs). After about 70 years out of reactor, the contribution of the actinides to thermal power exceed that of the fission products.

This tendency can be observed in the ingestion toxicity profiles shown in **Figure 3**. The short-lived radio nuclides (^{90}Sr and ^{137}Cs) significantly contribute to the health risk of used nuclear fuel until several decades and the TRUs contribute to the most of the health risk after about 1000 years of discharge (**Table 2**).

On the contrary to ^{90}Sr and ^{137}Cs, ^{99}Tc and ^{129}I are long lived fission products but also important species because of their significant amounts in the fission products (**Table 3**) and solubility in common underground water. They are relative easy to migrate from geological repository to ground and threat long term integrity of the repository.

ULSAN NATIONAL INSTITUTE OF
SCIENCE AND TECHNOLOGY

If we can separate each group of used nuclear fuel, we can reduce the radioactivity and decay heat of final waste and lower disposal criteria (**Figure 1**. (b)). In addition, the U and TRUs can be reused as energy resources in the Sodium Fast Reactor (SFR). Seoul National University studied a way to reduce HLW (High Level Waste) which is defined as alpha emitter activity concentration higher than 4000 Bq/g and heat generation higher than $2\mathrm{kW/m^3}$ to ILW (Intermediate Level Waste) satisfying disposal criteria of WIPP (Waste Isolation Pilot Plant) which is a geological repository for ILW successfully operated from 1999 in the USA [2].

ULSAN NATIONAL INSTITUTE OF
SCIENCE AND TECHNOLOGY

Table 1. The used nuclear fuel storing status in South Korea (The 1st quarter of the 2018) [1].

Site	Type (Numbers)	Storage Capacity (Bundle)	Cumulative Volume (Bundle)	Percentage (%)
Wolsong	HWR (4)	169632	125480	74.0
	LWR (2)	1046	317	30.3
	Dry storage	330000	313200	94.9
Kori	LWR (6)	8115	6081	74.9
Saeul	LWR (1)	780	100	12.8
Hanbit	LWR (6)	9017	6103	67.7
Hanul	LWR (6)	7066	5263	74.5

ULSAN NATIONAL INSTITUTE OF SCIENCE AND TECHNOLOGY

(a)

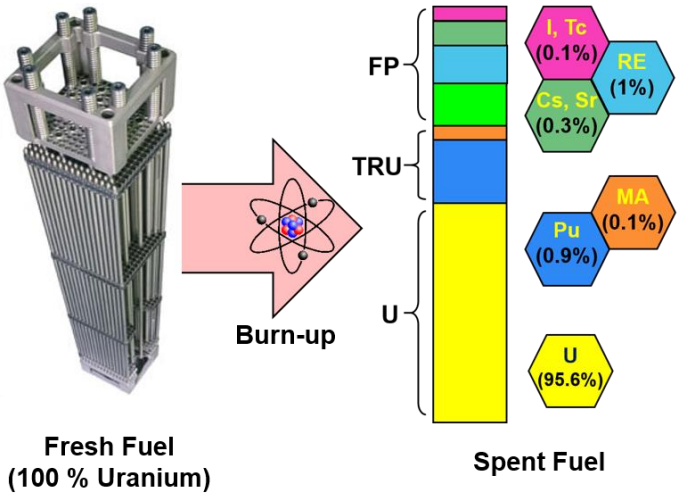

(b)

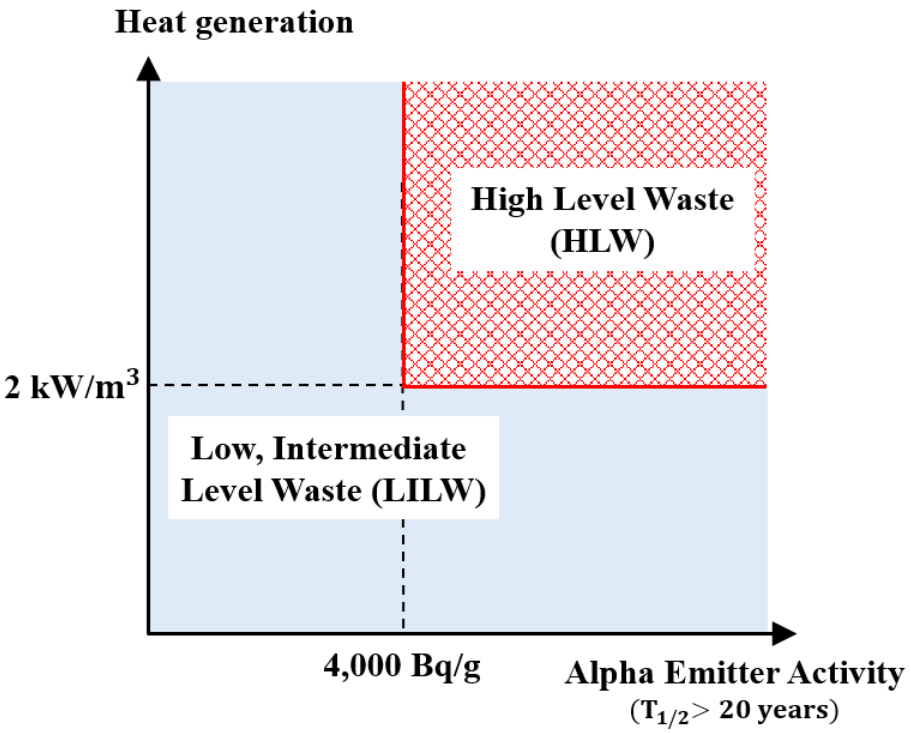

Figure 1. (a) Composition of used nuclear fuels (33,000 MWD/MT, 10 years cooling). (b) The classification of radioactive waste in South Korea.

ULSAN NATIONAL INSTITUTE OF
SCIENCE AND TECHNOLOGY

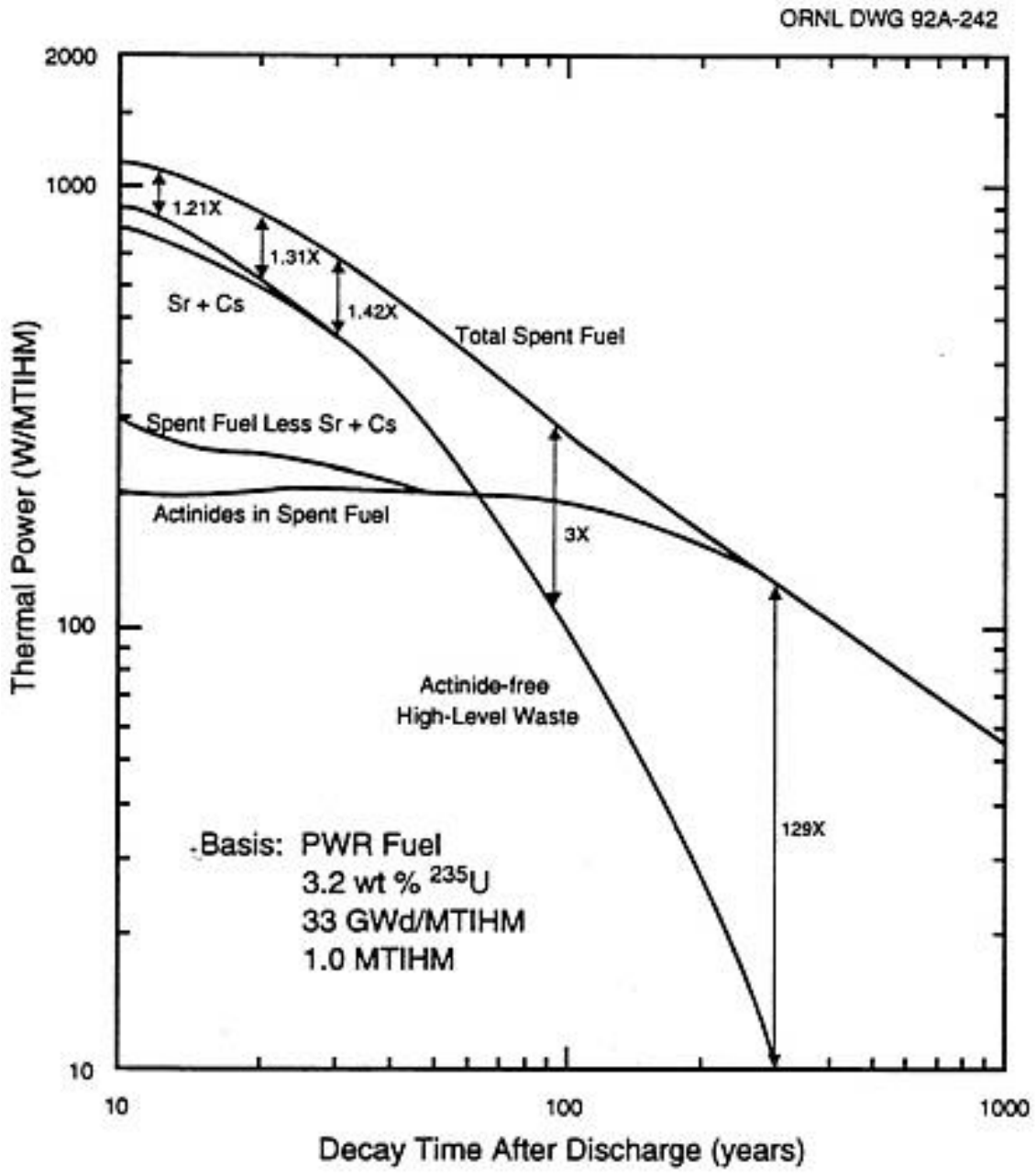

Figure 2. Thermal power profiles of spent LWR fuel and its major constituents groups [3].

ULSAN NATIONAL INSTITUTE OF SCIENCE AND TECHNOLOGY

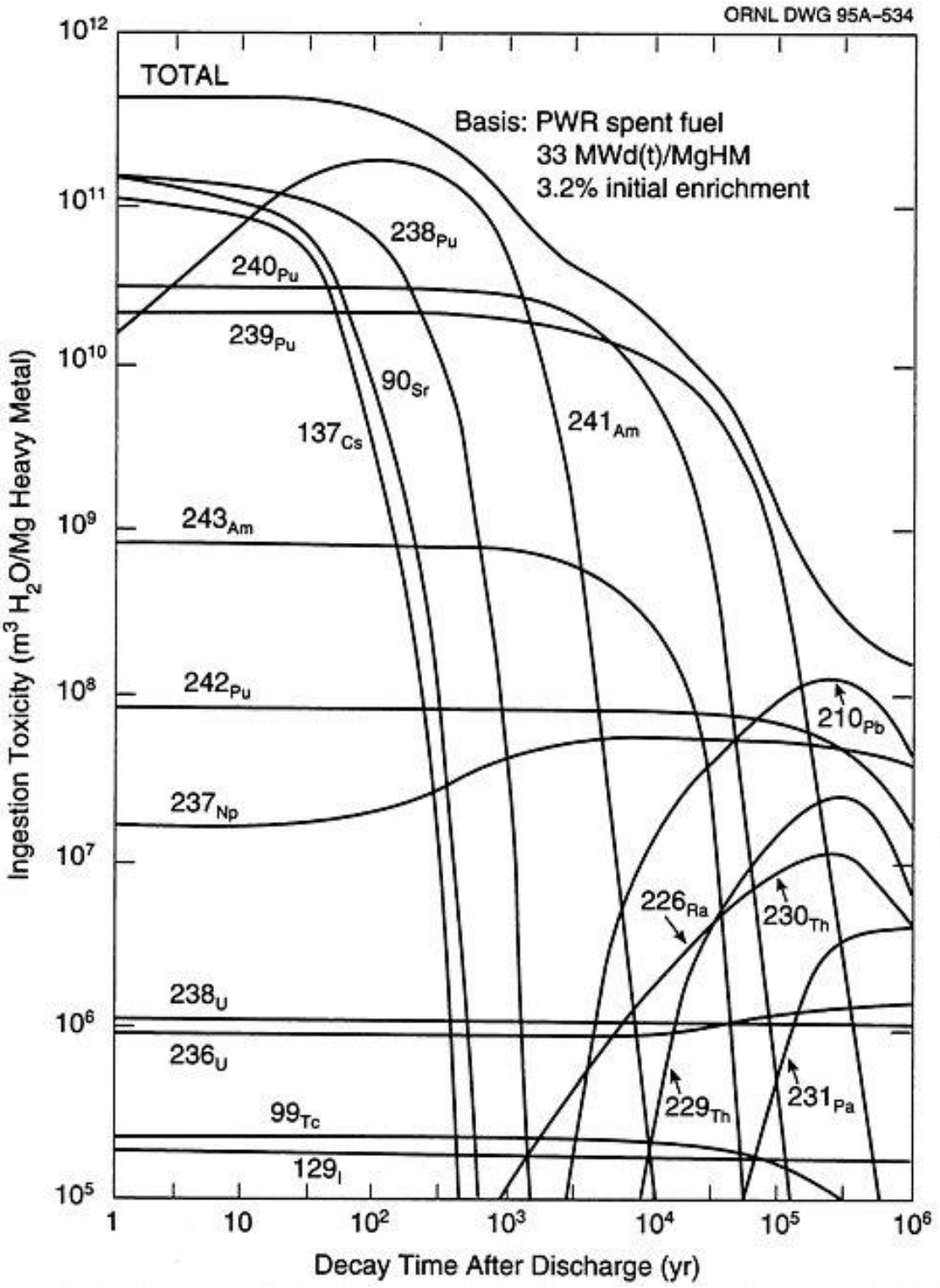

Figure 3. Toxicity from ingestion as a function of decay time for a number of nuclides in spent LWR fuel. [4].

ULSAN NATIONAL INSTITUTE OF SCIENCE AND TECHNOLOGY

Table 2. Properties of actinides in discharged uranium fuel (Uranium-fueled PWR, 1000 MWe, 150 days after discharge) [5].

Nuclide		Half-Life	kg	Ci
U	^{234}U	2.47×10^5 yr	3.14	19.4
	^{235}U	7.10×10^8 yr	215	4.61×10^{-1}
	^{236}U	2.39×10^7 yr	114	7.22
	^{237}U	6.75 days	9.15×10^{-7}	74.7
	^{238}U	4.51×10^9 yr	2.57×10^4	8.56
Np	^{237}Np	2.14×10^6 yr	20.4	14.4
	^{239}Np	2.35 days	2.05×10^{-6}	478
Pu	^{236}Pu	2.85 yr	2.51×10^{-4}	134
	^{238}Pu	86 yr	5.99	1.01×10^5
	^{239}Pu	2.44×10^4 yr	144	8.82×10^3
	^{240}Pu	6.58×10^3 yr	59.1	1.30×10^4
	^{241}Pu	13.2 yr	27.7	2.81×10^6
	^{242}Pu	3.79×10^5 yr	9.65	37.6
Am	^{241}Am	458 yr	1.32	4.53×10^3
	^{242m}Am	141 yr	1.19×10^{-2}	116
	^{243}Am	7.95×10^3 yr	2.48	477
Cm	^{242}Cm	163 days	1.33×10^{-1}	4.40×10^5
	^{243}Cm	32 yr	1.96×10^{-3}	90.3
	^{244}Cm	17.6 yr	9.11×10^{-1}	7.38×10^4
	^{245}Cm	9.30×10^3 yr	5.54×10^{-2}	9.79
	^{246}Cm	5.50×10^3 yr	6.23×10^{-3}	1.92

ULSAN NATIONAL INSTITUTE OF SCIENCE AND TECHNOLOGY

Table 3. Properties of selected fission products of interest in used nuclear fuel and HLW [5].

Nuclide	Half-Life	Atoms per Fission Product Pair Produced	Thermal Cross Section (barns)
^{99}Tc	2.12×10^{5} yr	5.77×10^{-2}	44.4
^{129}I	1.57×10^{7} yr	1.07×10^{-2}	37.4
^{90}Sr	28.8 yr	4.43×10^{-2}	1.34
^{137}Cs	30.2 yr	60.2×10^{-2}	1.76×10^{-1}

ULSAN NATIONAL INSTITUTE OF SCIENCE AND TECHNOLOGY

1.2 Pyroprocessing

Pyroprocessing is a dry reprocessing technique for used nuclear fuel. The heat generation and radioactivity of used nuclear fuel can be significantly reduced by the pyroprocessing. Short-lived high radioactive elements and long-lived ground water soluble fission products from used nuclear fuel can be separated by the pyroprocessing. In addition, U and TRUs can be separated and reused in the Sodium Fast Reactor (SFR). At the same time, pyroprocessing has intrinsic proliferation resistance because the selective separation of Pu is difficult. The TRUs have similar electrochemical properties in molten salt and they are co-deposited on the liquid cadmium cathode in electrorefining process.

Pyroprocessing consists of head-end processes (decladding, voloxidation, oxide feed preparation) which separate used nuclear fuels from the cladding and vaporize radioactive volatile elements like Tc, Cs, and I, and electrochemical processes (oxide reduction, electrorefining, electrowinning) which reduce metal oxides to metal form and separates U and TRUs from other fission products and the molten salt, and waste treatment processes as shown in **Figure 4**.

In this work, we focused on the electrochemical processes in which the separation of nuclear materials occur. These electrochemical systems is usually composed of electrodes where redox reactions occur by applied current and potential, electrolyte through which ions are transferred, and agitators which accelerate mass transfer by causing hydrodynamic motion in the electrolyte.

1.2.1 Oxide reduction process

After the head-end processes, the elements of used nuclear fuel exist in oxide forms. Oxide reduction process produce metal from these oxides by electrochemical reactions in LiCl-Li_2O electrolyte at 923 K. During this process, the used nuclear fuel oxides are dissolved into the molten salt in chloride form and they are deposited on the cathodic electrode by applied current or potential. However, the short-lived high radioactive fission products remained in the molten salt because of their thermodynamic stability in chloride form. The metallization of oxides to more dense metals and separation of high radioactive fission products reduce the volume, heat, and radioactivity of the products [6]. The metal products directly transferred to the electrorefining process.

1.2.2 Electrorefining & Electrowinning process

The electrorefining process is the most important process in the pyroprocessing, because the separation of nuclear materials is conducted during this process. The metal products from the oxide reduction process are loaded into the anode basket and they are dissolve into the LiCl-KCl eutectic molten salt at 773 K. Among the dissolved metal chlorides, pure U is recovered on a solid cathode in the electrorefining process.

ULSAN NATIONAL INSTITUTE OF
SCIENCE AND TECHNOLOGY

After the electrorefining process, U and TRUs and fission products remain in the used molten salt. During the electrowinning process, these remaining nuclear materials are co-deposited on the liquid cadmium cathode (LCC) which means the sole separation of Pu is impossible. This a key characteristic of pyroprocessing which has intrinsic proliferation resistance, on the contrary to the aqueous reprocessing. Argonne National Laboratory (ANL) has been developed electrorefining process incorporating the electrowinning process shown in **Figure 5**. This type of electrorefiner consist of solid cathode on which the pure U is deposited, liquid cadmium where the co-deposition of U and TRUs occurs.

ULSAN NATIONAL INSTITUTE OF
SCIENCE AND TECHNOLOGY

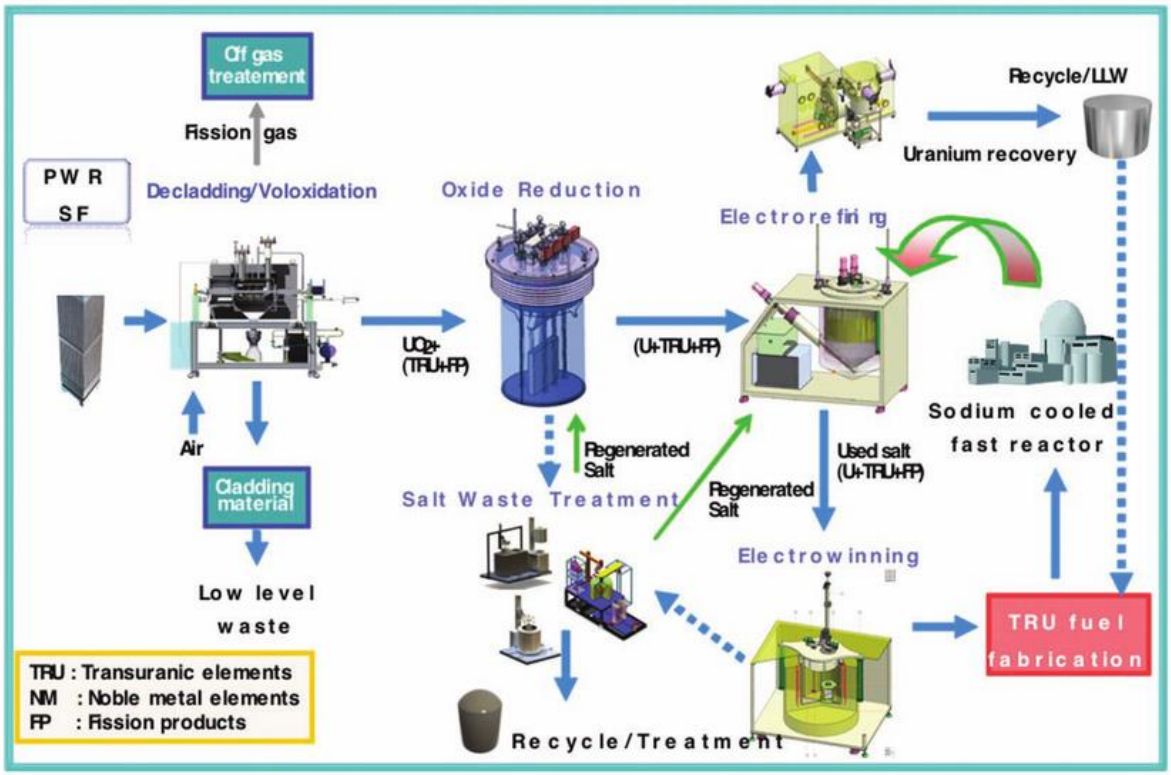

Figure 4. Flow diagram of pyroprocessing developed by KAERI [6].

ULSAN NATIONAL INSTITUTE OF
SCIENCE AND TECHNOLOGY

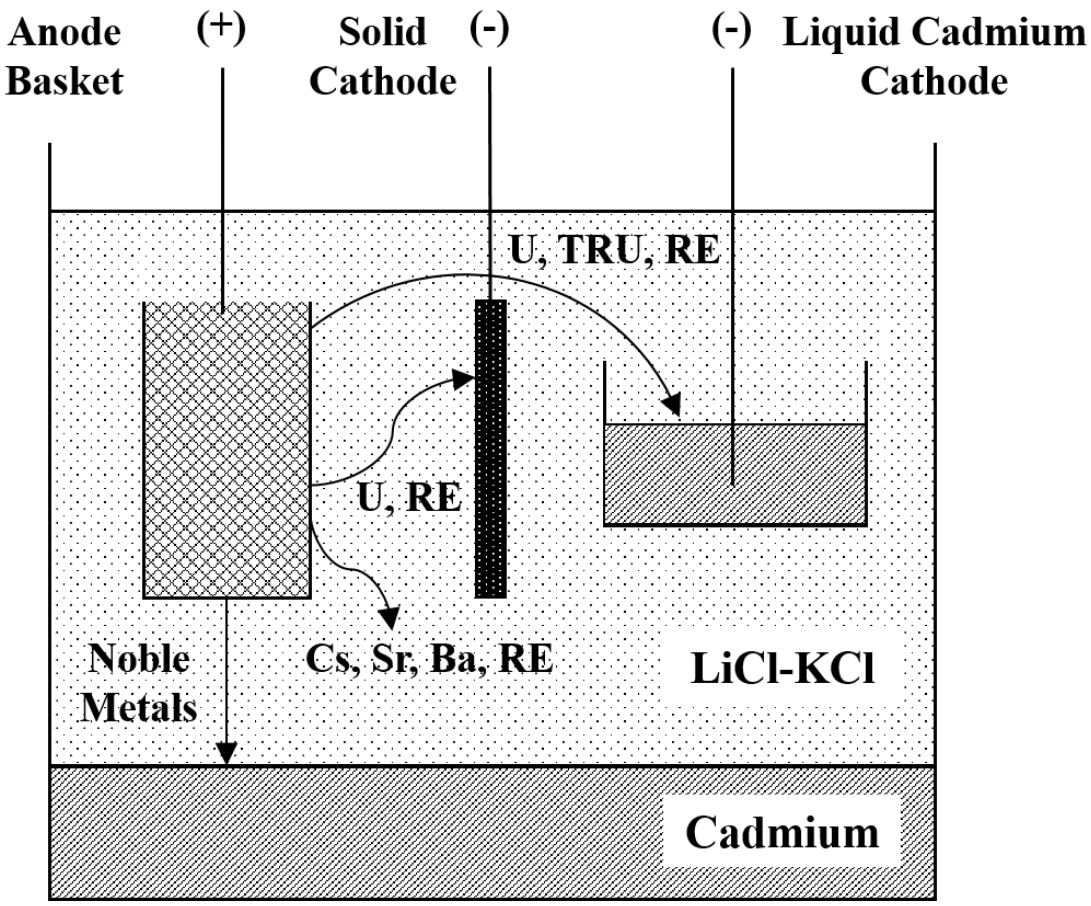

Figure 5. Schematic representation of the IFR electrorefining process [7].

ULSAN NATIONAL INSTITUTE OF
SCIENCE AND TECHNOLOGY

II. Literature Reviews

2.1 Hydrodynamic electrochemical system

Liquid metal electrodes are used in a wide range of applications including energy storage system [8-10] molten salt electrolysis of metals [11] and used nuclear fuel processing [12, 13]. These applications involve multiple elements with different chemical states (e.g., oxides and metals of actinide and lanthanide), and also various electrochemical media such as molten salts and solid and liquid electrodes [14]. In addition, rotating solid electrodes and complicated hydrodynamic stirrers are sometimes introduced in the process to enhance the mass transfer of ions from the bulk electrolyte to the electrode [15-18]. Most industrial processes use hydrodynamic accelerations for mass transfer. Understanding the multiple physical phenomena involved in this process is crucial to implement a cost-effective process that optimizes operating conditions and cell configuration.

2.2 Computational modeling of electrorefining process

The electrorefining process is one of the hydrodynamic electrochemical system dealing with nuclear materials and radioactive elements. Because of the high radioactivity and decay heat generated from the used nuclear fuel, the experimental optimization of the electrorefining process is costly and dangerous. Therefore, computational modeling of electrorefining process have been developed to optimize the operating conditions of electrorefining process. In addition, the computational modeling can be utilized to predict composition of electrode products and electrolyte.

Johnson [19] developed a thermodynamic model for electrorefining processes which involve the transport of the U and Pu from one liquid alloy to another through a molten salt. Nawada et al. [20] also developed a thermochemical model for electrotransport of U and Pu in an electrorefiner. The difference between modeling with concentration dependent and concentration independent activity coefficients for U and Pu in liquid cadmium were also investigated. In addition, the electrotransport to a solid cathode and anodic dissolution were simulated in this model. Ghosh et al. [21] developed a model, PRAGAMAN, based on the thermodynamic equilibrium at the interfaces of electrodes and molten salt. **Figure 6** shows the effect of minor actinides and rare earths element to the electrotransport behaviors of U and Pu. The rate of electrotransport of U and Pu shows significant increase when the rare earth chlorides exist in the molten salt.

ULSAN NATIONAL INSTITUTE OF
SCIENCE AND TECHNOLOGY

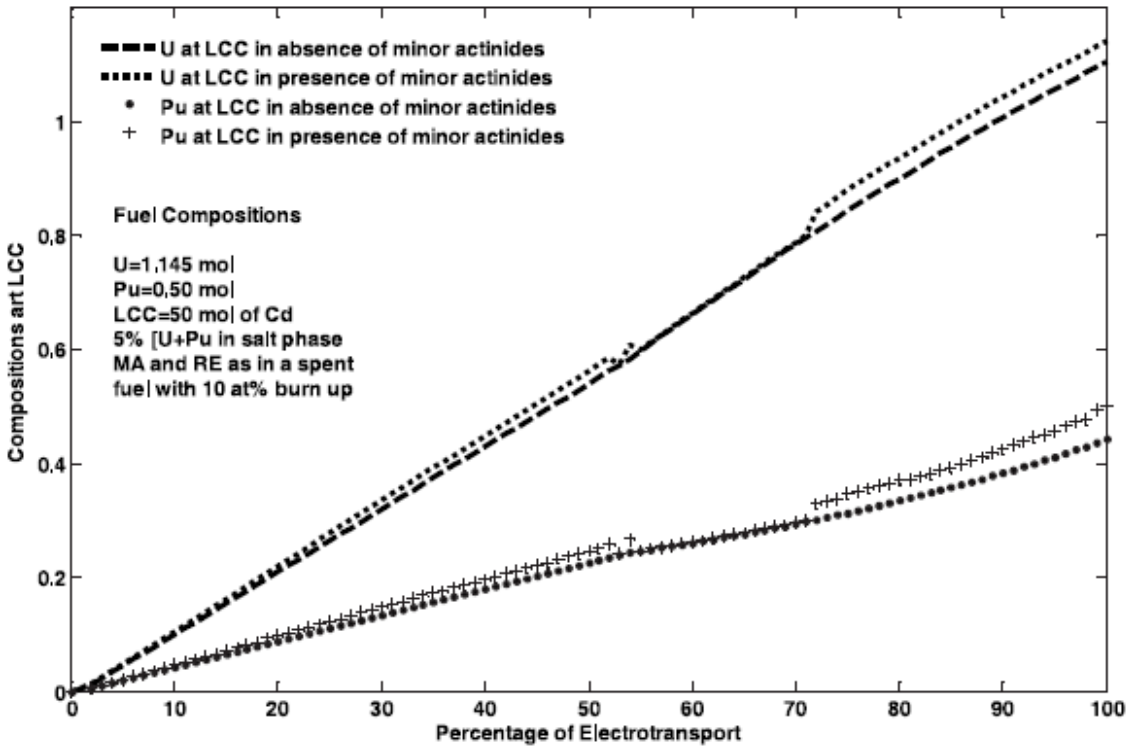

Figure 6. Comparison of U and Pu electrotransport profile in absence and presence of minor actinides and rare earths [21].

ULSAN NATIONAL INSTITUTE OF SCIENCE AND TECHNOLOGY

Kobayashi et al. [22] developed a simulation code, TRAIL which employed constant diffusion layer thickness near the electrodes. This model assumed uniform concentration of the elements in the molten salt and cadmium anode, except in the vicinity of the electrode interfaces. The linear concentration gradient was assumed in the diffusion layer as shown in **Figure 7**. The comparisons of experimental polarization data and modeling results with various diffusion layer thickness in the molten salt and liquid cadmium anode are shown in **Figure 8**. They found that modeling result with 0.002 cm of diffusion layer thickness shows the closest result with experimental result in both electrodes.

Hoover et al. [23] developed a 1D model for the Mark-IV electrorefiner. This model calculated electrokinetics equations, Nernst equation (1) which calculates equilibrium potential at the anode-salt interface relative to a reference electrode and Butler-Volmer equation (2) which calculates the current passes through the anode-salt interface caused by the surface overpotentials to investigate the dissolution rate of U, Pu, and Zr at the anode.

$$E_i = E_i^0 + \frac{RT}{n_i F} ln\left(\gamma_i X_{i,s}\right) \quad (1)$$

Here, R is the ideal gas constant, T is the operating temperature, n_i is the charge of species i, F is the Faraday constant, γ_i is the activity coefficient of species i, and $X_{i,s}$ is the mole fraction of species i in the salt next to the interface.

$$I_i = i_0 A_t \left(exp\left(\frac{n_i \alpha F}{RT}\eta_{i,s}\right) - exp\left(-\frac{n_i(1-\alpha)F}{RT}\eta_{i,s}\right)\right) \quad (2)$$

Here, I_i is the total current of species i arising at the electrode, i_0 is the exchange current density, A_t is the surface area of the electrode, α is the transfer coefficient, and $\eta_{i,s}$ is the surface overpotential of species i at the interface.

Hoover et al. conducted a prediction of the total anode potential and validation by the experimental data sets provided by Idaho National Laboratory (INL). The experiment was conducted with varying applied current as shown **Figure 9**. (a), (b). The **Figure 9**. (c), (d) shows the comparison of the anode voltage between predicted result by the proposed model and experimental result for DT1 and DT2. The predicted results and measured results of anode potential were well matched to each other. They also calculated the partial currents of U, Pu, and Zr (**Figure 10**). The most of the applied current was used in oxidizing small amount of Pu (< 0.25 wt.%) because of highly negative potential of Pu. After, the Pu is exhausted, U becomes the primary species occupying the oxidizing current throughout most of the electrorefining process.

ULSAN NATIONAL INSTITUTE OF
SCIENCE AND TECHNOLOGY

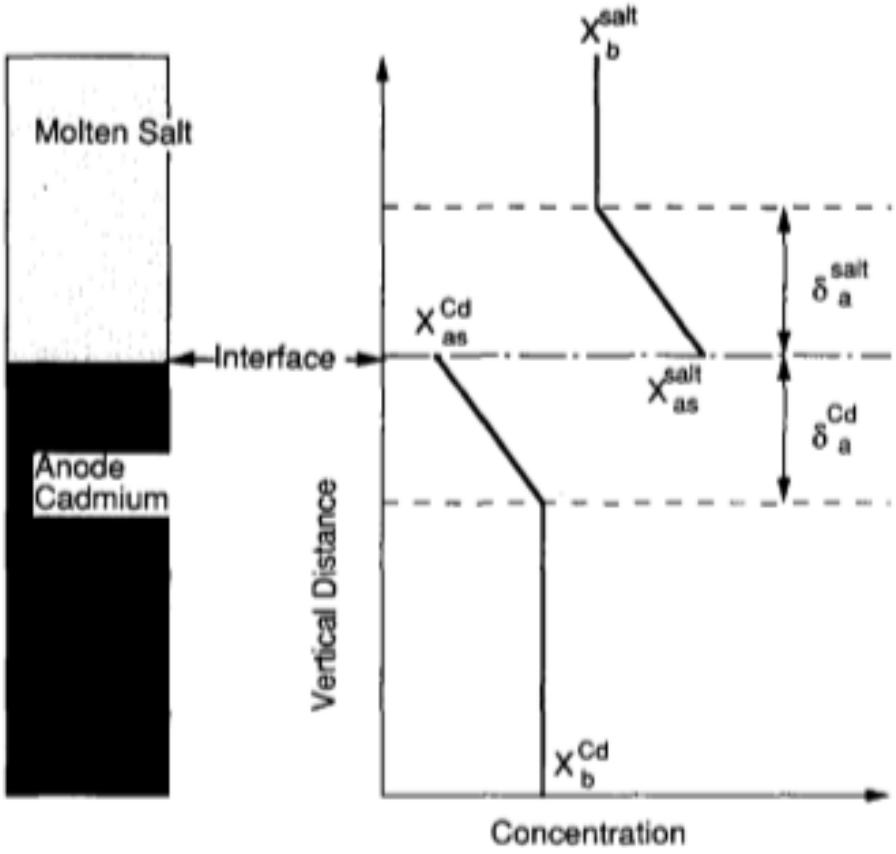

Figure 7. Diffusion layer model for the Cd anode [22].

ULSAN NATIONAL INSTITUTE OF
SCIENCE AND TECHNOLOGY

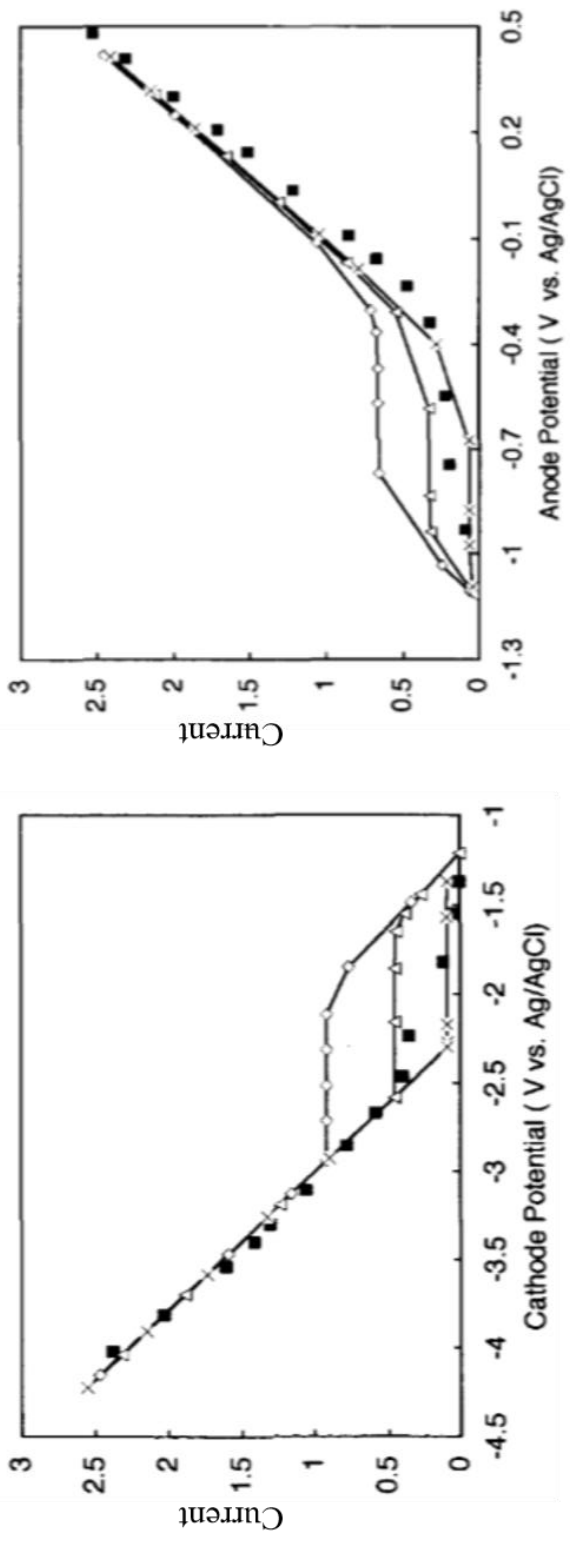

Figure 8. (a) Cathode polarization curve for a U concentration of 0.75 wt.% in the salt. (b) Anodic polarization curve for U concentration of 0.02 wt.% in the cadmium measured in the 10 g scale ER, compared with calculated curves for diffusion layer thickness, δ (cm) of 0.001 (◇), 0.002 (△) and 0.01 (x) [22].

ULSAN NATIONAL INSTITUTE OF SCIENCE AND TECHNOLOGY

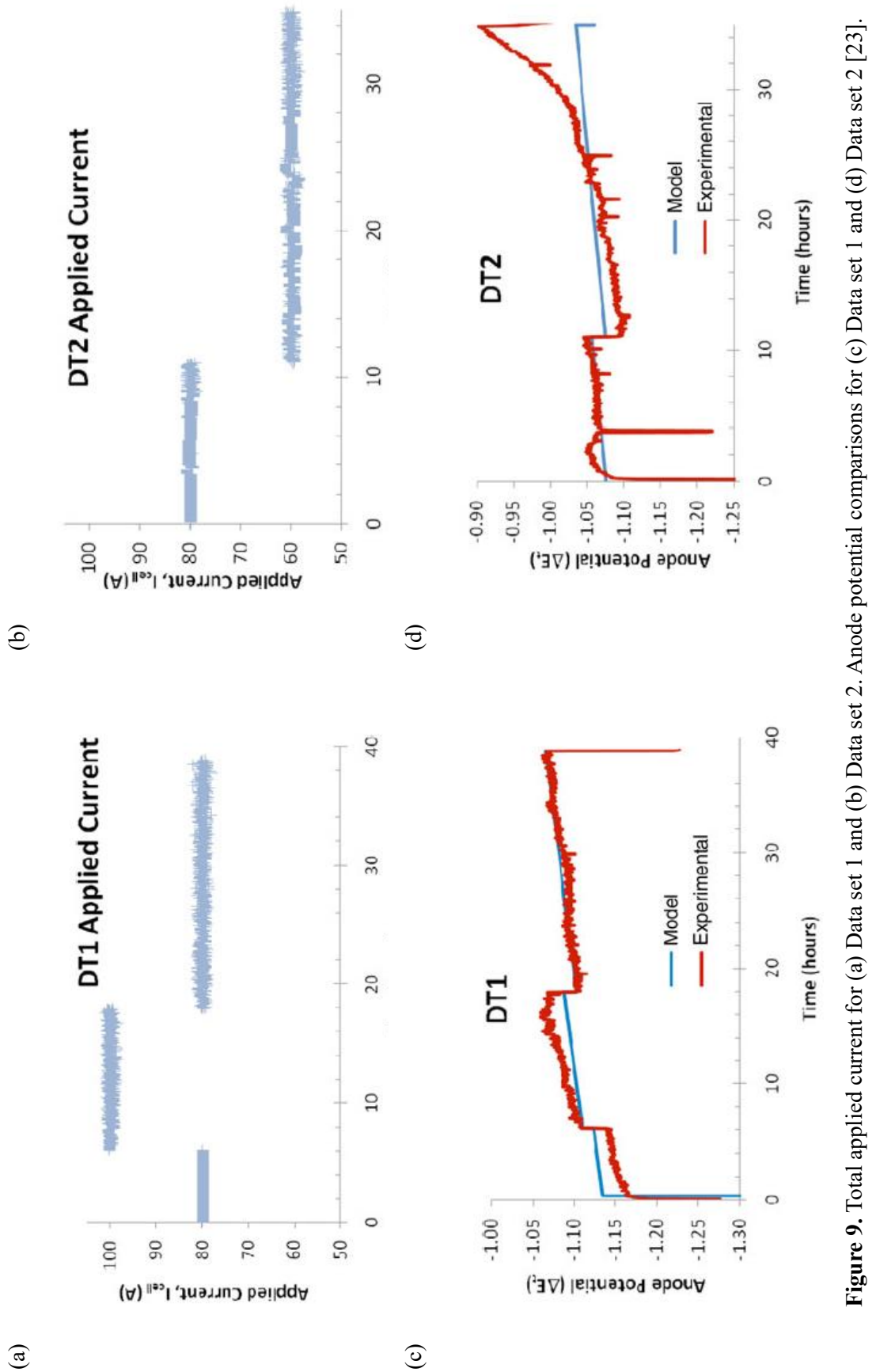

Figure 9. Total applied current for (a) Data set 1 and (b) Data set 2. Anode potential comparisons for (c) Data set 1 and (d) Data set 2 [23].

ULSAN NATIONAL INSTITUTE OF
SCIENCE AND TECHNOLOGY

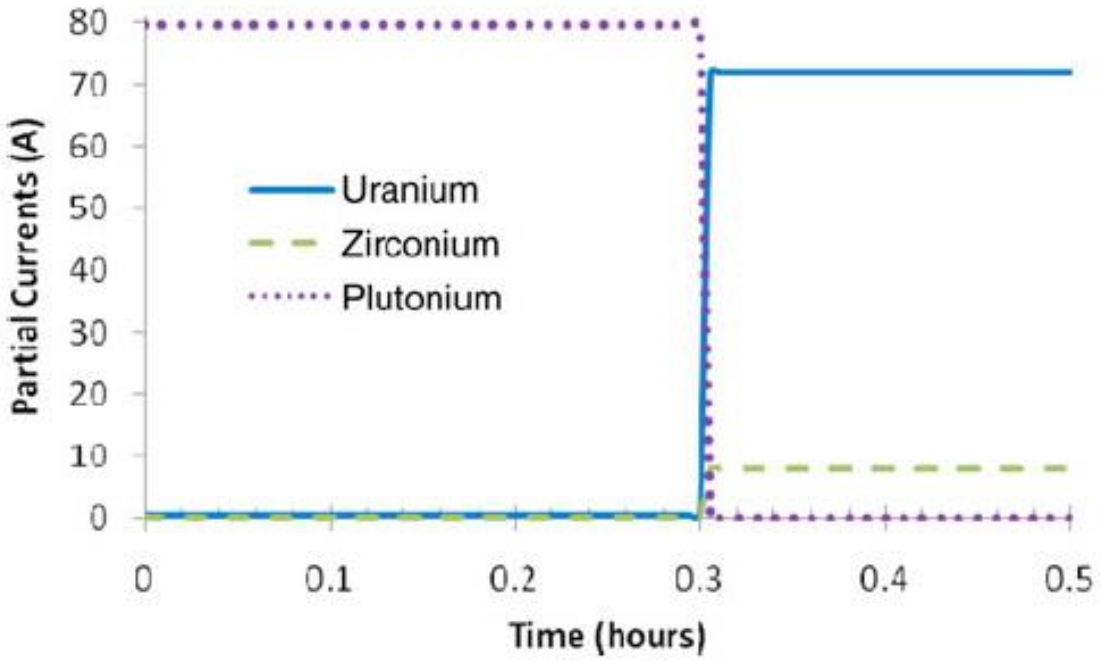

Figure 10. The prediction of partial currents during the first half-hour of dissolution in the Mark-IV electrorefiner [23].

ULSAN NATIONAL INSTITUTE OF SCIENCE AND TECHNOLOGY

Zhang, Srihari et al., and Seo et al. [14, 24, 25] developed kinetic models for lab-scale electrorefining process with constant diffusion layer thickness (0.002 cm) from the TRAIL model [22]. They successfully predicted the concentration profiles of multi-components in the electroreining process and the simulated results were validated by the experimental results of the ANL [26]. Zhang's 1D model considered the changes of the surface areas and the volume of the electrodes were also considered in this model. Srihari et al. developed 2D model using COMSOL Multiphysics. They investigated the concentration changes of the molten salt and cadmium anode and metal deposition on the solid cathode. Seo et al. studied the effect of diffusion layer thicknesses, transfer coefficients, and difference of electrochemical potentials to the behaviors of electrochemical reactions for U and Pu. Cumberland et al. [27] developed a 1D transient electrorefiner model, ERAD, which developed the REFIN code by adding an anodic layer which is important in the processing of fuel with high zirconium content. They investigated optimized modeling parameters like, diffusion coefficients, standard potentials, and exchange current density by meta-analysis of reduction peaks of cyclic voltammetry for UCl_3 in LiCl-KCl molten salt.

Recently, several researchers have developed 3D computational models that fully couple electrochemistry and hydrodynamics. However, these models require extensive computational resources and suffer from a convergence problem in multi-species calculations [16, 28-32].

To overcome these problems, Bae et al. [33] developed a 3D hydrodynamic electrochemical model coupled with 1D electrochemical analysis model, REFIN for the lead-bismuth cooled fast reactor. The 3D model analyzed electrorefiner which consist of a fuel basket anode at the center and four solid cathodes in LiCl-KCl eutectic molten salt. There is one stirrer at the center, rotating at a speed of 60 rpm. The solid cylinders are also rotating at a speed of 10 rpm. Because the diffusion layer thickness is formed by the effect of fluid mechanics, the diffusion layer thickness was calculated in the 3D model in the way shown in **Figure 11**. (a). The calculated diffusion layer thickness is shown in **Figure 11**. (b). The value is in range from 45 μm to 51 μm.

Choi et al. [28] also developed a 3D-1D coupled model which shows the local current density distribution on the cathode for various electrode rotational speeds based on the Mark-IV electrorefiner. Shortly after, Choi et al. [29] developed 3D electrorefining model, calculating cell potentials with respect to various real anode surface area cases. However, they found local inconsistencies between the simulated results and experimental results.

ULSAN NATIONAL INSTITUTE OF
SCIENCE AND TECHNOLOGY

(a)

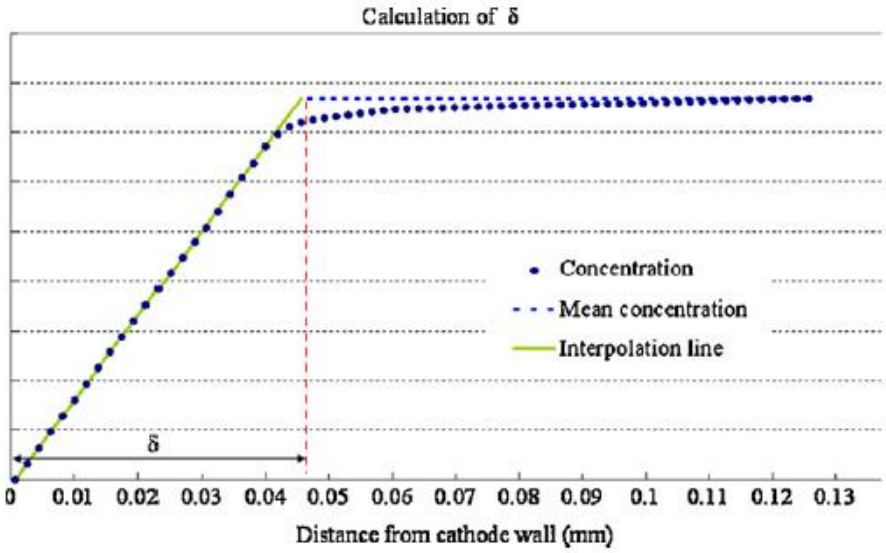

(b)

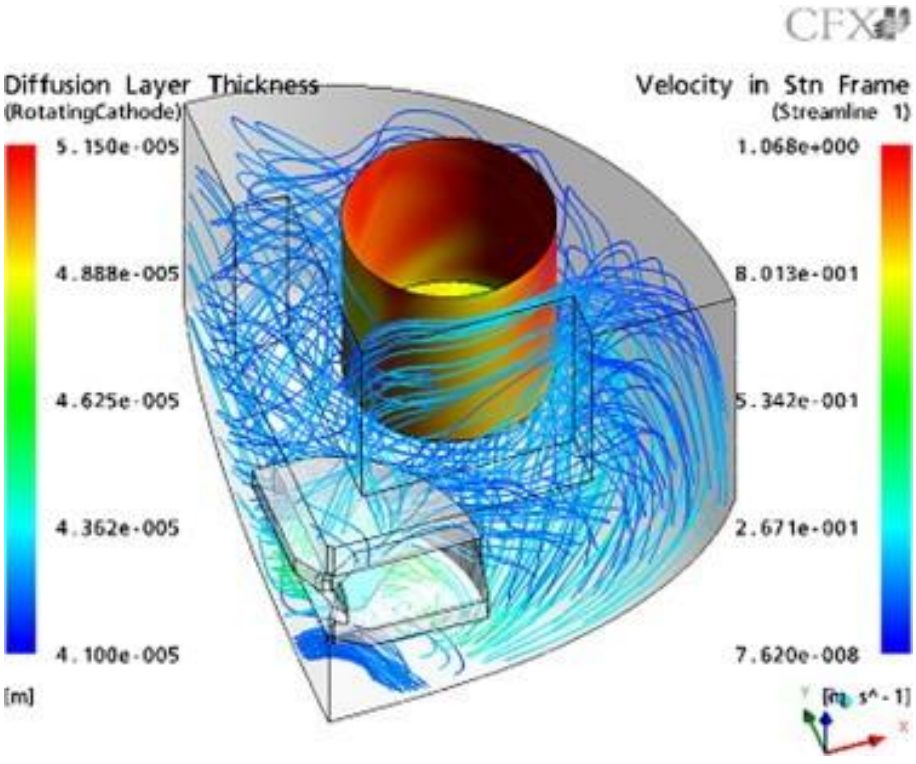

Figure 11. (a) Calculation method of the diffusion layer thickness. (b) Three-dimensional distribution of the diffusion layer thickness near cathode [33].

ULSAN NATIONAL INSTITUTE OF
SCIENCE AND TECHNOLOGY

2.3 Reference Experiment

There are only few open data about electrorefining experiment with nuclear materials. Tomcuzk et al. [26] conducted a lab-scale electrorefining experiment using actinides and fission products at a temperature of 773 K. Because the electrorefining cell consists of a mild steel solid cathode and liquid cadmium anode, the characteristics of solid and liquid electrode can be simultaneously investigated with this experiment. In addition, this experiment has been proven to be computationally reproducible by many electrorefining models. Therefore, the experiment of the ANL conducted by Tomcuzk et al. was considered as the benchmark to validate the proposed model.

2.3.1 Cell configuration

The ANL electrorefining cell (**Figure 12**) consisted of a LiCl-KCl eutectic salt, a liquid cadmium anode, a rotating mild steel cathode inside a mild steel crucible with a height of 30.2 cm and a diameter of 15.2 cm. However, the specific size of each component was not provided in the ANL report. Therefore we referred to the size of details in other literature [22]. The liquid cadmium anode occupied the bottom 10.3 cm of the crucible, and molten LiCl-KCl eutectic salt occupied 11.3 cm of depth above the liquid cadmium. The cathode, with a height of 7.5 cm and a diameter of 3.2 cm, was in contact with the LiCl-KCl molten salt, and the agitator was positioned at a sufficient depth to reach the liquid cadmium.

The molten salt region in contact with the cathode and anode (the region highlighted by the red line in **Figure 12**) was considered in the computational model. Although an agitator itself was not included the computational domain, the effects of the agitator were considered by introducing a constant diffusion boundary layer thickness at the interface between molten salt and liquid metal in the computational domain.

ULSAN NATIONAL INSTITUTE OF
SCIENCE AND TECHNOLOGY

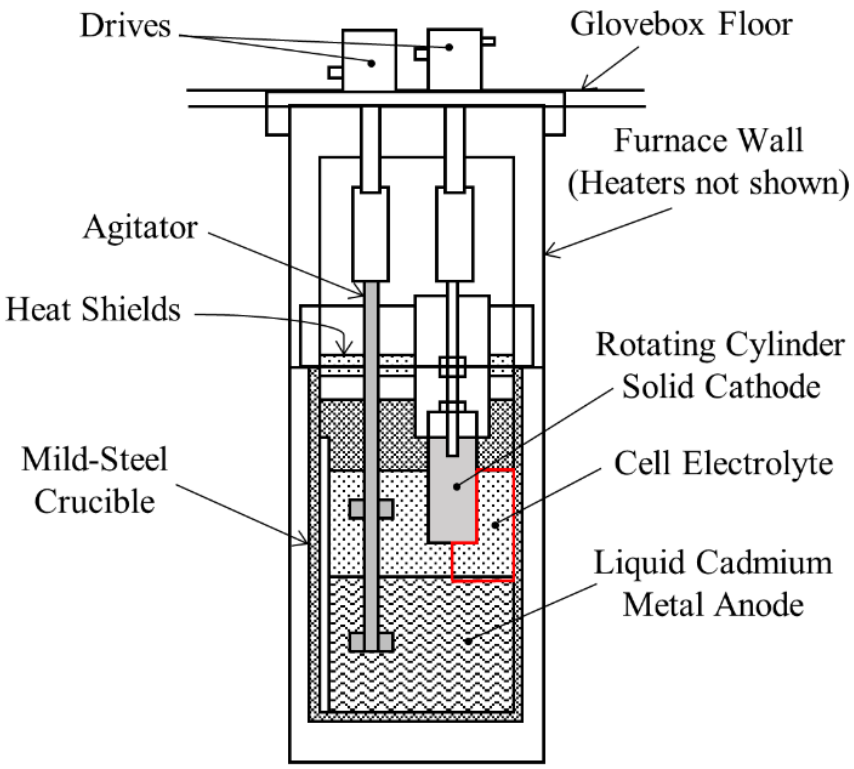

Figure 12. Schematics of the Argonne National Laboratory electrorefining experimental cell: the region outlined in red was considered in the proposed computational model [26]. U, Pu, and Nd are dissolved from a liquid cadmium anode at the transported to the LiCl-KCl molten salt at 773 K, and deposited on the cathode surface; a rotating solid cylinder cathode produce hydrodynamic motions and accelerate mass transfer.

ULSAN NATIONAL INSTITUTE OF SCIENCE AND TECHNOLOGY

2.3.2 Operating conditions and experimental results

During the ANL's experiment, five tests were conducted in the electrorefining cell and their experimental conditions are summarized in **Table 4**. Each test was conducted with a different constant current and an operating time at a temperature of 773 K. During the operation, the cathode was rotating at a speed of 35 rpm.

The cathode products, anode metal, and salt samples were analyzed before each test. The results of analysis are summarized in **Table 5**. The initial ANL electrorefining cell contained 3.680 kg (1.808 L) of LiCl-KCl molten salt and U and Pu at 1.610 and 1.818 wt%, respectively, in tri-chloride form. U and Pu were present at 1.014 and 0.592 wt%, respectively, in the initial 16.5 kg (2.050 L) liquid cadmium anode. In addition, Ce, Y, and Nd were present at a total of 1.24 wt% in the molten salt in chloride form, and their concentrations in the cadmium anode were less than the detection limit of approximately 0.01 wt% [26].

The liquid metal U and Pu were oxidized into the molten salt and the concentration of liquid metal U and Pu in the cadmium anode decreased as additional tests were repeated. The U^{3+} and Pu^{3+} ions in the molten salt were reduced and deposited on the cathode. However, the composition of cathode deposit metal did not include much Pu in the early test numbers (1–3). Thereby, the concentration of Pu^{3+} in the molten salt increased because of active oxidation reactions at the anode and almost no reduction reactions at the cathode. When the limiting current of U^{3+} failed to satisfy the total applied current, the electrode potential became increasingly negative and the reduction current of Pu^{3+} started to increase.

2.3.3 Data assumed for computational model based on the ANL results

The initial conditions and results of the ANL electrorefining experiment were used in our computational model. However, the applied current and operating time of each test were not specified in the ANL report. Therefore, we assumed the operating current to be 1.45 A throughout all tests. Based on the assumed current and the amount of charge needed to deposit the total amount of U and Pu metal on the cathode (**Table 5**). we calculated the operating time of each test, assuming that the current efficiency was 100% as equation (3).

$$t = \sum_i \frac{n_i N_A m_i e}{M_i I} \tag{3}$$

Here, t is the operating time (s), n_i is the charge of species i (dimensionless), N_A is the Avogadro constant (mol^{-1}), m_i is the mass of deposited metal on the cathode of species i (g), e is the elementary charge, M_i is the molar mass of species i ($g\ mol^{-1}$), and I is the applied current (A). Furthermore, the results of Test 1 were used as the initial conditions for our 2D competitive reaction model; hence, the

ULSAN NATIONAL INSTITUTE OF
SCIENCE AND TECHNOLOGY

amounts of metals deposited in Test 1 were treated as zero values. Test 2 demonstrated the composition of the electrorefining cell after 22.46 hours of operation, and Tests 3, 4, and 5 demonstrated the cell compositions after an additional 17.70, 27.53, and 34.21 hours of operation, respectively.

ULSAN NATIONAL INSTITUTE OF SCIENCE AND TECHNOLOGY

Table 4. Operating conditions for each the Argonne National Laboratory lab-scale electrorefining test [26].

	Test number				
	1	2	3	4	5
Temperature (K)	773				
Cathode rotating speed (rpm)	35 (counterclockwise)				
Applied current (A)	2-5	1.5-2	2	1	1
Maximum voltage (V)	-0.13	-0.10	-0.12	-0.10	-0.26
Minimum voltage (V)	-0.21	-0.17	-0.17	-0.27	-0.46
Estimated operating time (h)*	22.46	17.70	9.825	6.689	-

* Operating time is estimated from the ANL experimental results based on the total charge transferred to the cathode in relation to the amount of deposited metal.

ULSAN NATIONAL INSTITUTE OF
SCIENCE AND TECHNOLOGY

Table 5. Experimentally measured results of material compositions after each test of the Argonne National Laboratory lab-scale electrorefining experiment [26]. No initial conditions available, so benchmark is simulated right after test number 1.

	Test number				
	1	2	3	4	5
U in cadmium pool (wt%)	1.014	0.373	0.235	0.048	0.012
Pu in cadmium pool (wt%)	0.592	0.538	0.465	0.392	0.270
Ce, Nd, and Y in cadmium pool (wt%)	< 0.01	< 0.01	< 0.01	< 0.01	< 0.01
U in salt after test (wt%)	1.610	1.119	0.595	0.243	0.081
Pu in salt after test (wt%)	1.818	2.193	2.764	3.163	3.211
Ce, Nd, and Y in salt after test (wt%)	1.24	1.24	1.24	1.24	1.24
U in deposited metal (g)	70.91*	96.40	75.97	41.72	16.28
Pu in deposited metal (g)	0.02*	0.04	0.00	0.47	12.75

* Indicates a value treated as zero because Test 1 was considered as an initial condition.

ULSAN NATIONAL INSTITUTE OF
SCIENCE AND TECHNOLOGY

III. Numerical Model

This paper combines a 3D hydrodynamic model with a 2D multi-species electrochemical model to mitigate the computational costs and address the convergence problem in a fully coupled 3D model. The capability of the developed model is validated in comparison with the lab-scale electrorefining experiments involving actinides and fission products performed by the Argonne National Laboratory (ANL) using a liquid metal anode and rotating solid cylinder cathode in a LiCl-KCl electrolyte [26]. The electrolyte and liquid metal regions, where the mass transfer of the ions is mostly determined by diffusion, are estimated by the 3D hydrodynamic model, and the diffusion of ions in those regions and electrochemical reactions are calculated by the 2D model. Using the proposed computational model, competitive anodic and cathodic reactions among two actinides elements (U and Pu) and a rare earth element (Nd) were simulated, and the amount of cathode deposits are compared to the experimental results.

3.1 Mathematical equations

3.1.1. Mass transfer

The net charge of positive ions and negative ions is balanced in the molten salt and therefore the whole electrorefining cell is neutral. The concentration of each species is conserved throughout the calculation according to equation (4).

$$\frac{\partial c_i}{\partial t} + \nabla \cdot N_i = 0 \tag{4}$$

Here, C_i is the concentration of species i (mol cm^{-3}), N_i is the mass flux of species i (mol s^{-1} cm^{-2}). The mass flux is governed by the Nernst-Plank equation which is a combination of diffusion, convection, and electromigration. Because the system contains sufficient supporting electrolyte, we could neglect the electromigration term in our computational model.

$$N_i = -D_i \nabla C_i + C_i v - \frac{n_i F}{RT} D_i C_i \nabla \phi \tag{5}$$

Here, D_i is the diffusion coefficient of species i (cm^2 s^{-1}), v is the velocity of the molten salt medium (m s^{-1}), n_i is the charge of species i, F is Faraday's constant (C mol^{-1}), R is the gas constant (J mol^{-1}K^{-1}), T is the temperature (K), and ϕ is the electric potential (V).

To reflect the rotation effect of the cathode, the Navier-Stokes equation for incompressible flow and constant viscosity (6) was implemented in the 3D model. The first, second, third, and fourth terms of equation (6) represent the inertial, pressure, viscous, and external forces, respectively. In the fluid

ULSAN NATIONAL INSTITUTE OF SCIENCE AND TECHNOLOGY

dynamic module of the 3D model, equation (7) was implemented together with the Navier-Stokes equation for continuity.

$$\rho\left(\frac{\delta v}{\delta t} + v \cdot \nabla v\right) = -\nabla p + \nabla \cdot \mu(\nabla v + (\nabla v)^T) + f \quad (6)$$

$$\frac{\delta \rho}{\delta t} + \nabla \cdot (\rho v) = 0 \quad (7)$$

Here, ρ is the fluid density (g cm^{-3}), v is the fluid velocity (m s^{-1}), p is the fluid pressure (Pa), μ is the fluid dynamic viscosity (N s m^{-2}), and f is the external forces applied to the fluid (F). The properties of the fluid used in the 3D model are summarized in **Table 6**.

ULSAN NATIONAL INSTITUTE OF SCIENCE AND TECHNOLOGY

Table 6. Transport properties of U, Pu, and Nd in LiCl(59 mol%)-KCl(41 mol%) electrolyte and liquid Cd metal at 773K [28, 34-36].

Properties (unit)	Values
Molar mass (g mol^{-1})	68.1
Density (g cm^{-3})	1.55
Dynamic viscosity (N s m^{-2})	1.23×10^{-4}
Diffusion coefficient of U in molten salt (cm^2 s^{-1})	1.447×10^{-5}
Diffusion coefficient of Pu in molten salt (cm^2 s^{-1})	1.122×10^{-5}
Diffusion coefficient of Nd in molten salt (cm^2 s^{-1})	1.395×10^{-6}
Diffusion coefficient of U in liquid Cd metal (cm^2 s^{-1})	1.51×10^{-5}
Diffusion coefficient of Pu in liquid Cd metal (cm^2 s^{-1})	1.51×10^{-5}
Diffusion coefficient of Nd in liquid Cd metal (cm^2 s^{-1})	3.40×10^{-6}

ULSAN NATIONAL INSTITUTE OF SCIENCE AND TECHNOLOGY

3.1.2. Electrochemical reactions

The mass flux on the surface of the electrodes is given by equation (8). The cathode acts as a mass sink of positive ionic species because of the reduction current. Likewise, the anode acts as a mass source of positive ionic species because of the oxidation current.

$$N_i = \frac{i_{loc,i}}{n_i F} \tag{8}$$

Here, $i_{loc,i}$ is the local current density of species i (A cm^{-2}). The Butler-Volmer equation (9) is the most precise electrokinetics equation to predict the local current density.

$$i_{loc,i} = i_{ex,i}\{\frac{C_{s,i}^{ox}}{C_{b,i}^{ox}} exp\left(\frac{\alpha_i n_i F \eta_i}{RT}\right) - \frac{C_{s,i}^{red}}{C_{b,i}^{red}} exp\left(\frac{-\alpha_i n_i F \eta_i}{RT}\right)\} \tag{9}$$

Here, $i_{ex,i}$ is the exchange current density of species i (A cm^{-2}), $C_{s,i}^{ox}$ is the surface concentration of species i to be oxidized (mol m^{-3}), $C_{b,i}^{ox}$ is the bulk concentration of species i to be oxidized (mol m^{-3}), $C_{s,i}^{red}$ is the surface concentration of species i to be reduced (mol m^{-3}), $C_{b,i}^{red}$ is the bulk concentration of species i to be reduced (mol m^{-3}), α_i is the transfer coefficient of species i (dimensionless), and η_i is the overpotential of the electrode of species i (V).

In this computational model, modified Butler-Volmer equations that disregard the reverse reaction for both the cathode and anode are used. Equation (10) and (11) represent the local current density at the cathode and anode, respectively. These equations involve the concentration-dependent variables of equilibrium potential and limiting current. Especially equation (11) contains concentration term to reflect the effect of mass to the exchange current density across the liquid cadmium anode.

$$i_{loc,i} = -i_{ex,i} \frac{exp\left(\frac{-\alpha_i n_i F \eta_i}{RT}\right)}{1+\frac{i_{ex,i}}{i_{L,i}} exp\left(\frac{-\alpha_i n_i F \eta_i}{RT}\right)} \tag{10}$$

$$i_{loc,i} = i_{ex,i}\sqrt{C_{b,i}^{cd}} \frac{exp\left(\frac{\alpha_i n_i F \eta_i}{RT}\right)}{1+\frac{i_{ex,i}}{i_{L,i}} exp\left(\frac{\alpha_i n_i F \eta_i}{RT}\right)} \tag{11}$$

Here, $i_{L,i}$ is the limiting current density of species i (A cm^{-2}), $C_{b,i}^{cd}$ is the bulk concentration of species i in the liquid cadmium anode (mol m^{-3}), and α_i is the transfer coefficient of species i (dimensionless). The limiting current density is defined by equation (12). When the mass of reactant is not sufficient to satisfy the applied current, the reaction behaviors are started to be controlled by the mass.

$$i_{L,i} = \frac{n_i F D_i C_{b,i}}{\delta} \tag{12}$$

Here, δ is the thickness of diffusion dominant region (cm) and $C_{b,i}$ is the bulk concentration of species i (mol cm^{-3}).

ULSAN NATIONAL INSTITUTE OF SCIENCE AND TECHNOLOGY

The overpotential is defined as equation (13). It signifies the potential gap between an electrode and equilibrium potential for each species.

$$\eta_i = E - E_{eq,i} \tag{13}$$

Here, E is the electrode potential and $E_{eq,i}$ is the equilibrium potential for species i at the electrode surfaces.

The equilibrium potential is calculated by the Nernst equation which considers temperature, concentration, and activity coefficient of the species in the molten salt and cadmium anode. Equation (14) represents the equilibrium potential at the cathode. Because the reduced species at the interface of the cathode and electrolyte is solid-state, the reduction concentration and activity coefficient are simply treated as 1. Equation (15) represents the equilibrium potential at the anode.

$$E_{eq,i} = E_i^{\circ} + \frac{RT}{n_i F} ln\left(\gamma_{salt,i}\left[C_{b,i}^{salt}\right]\right) \tag{14}$$

$$E_{eq,i} = E_i^{\circ} + \frac{RT}{n_i F} ln\left(\frac{\gamma_{salt,i}\left[C_{b,i}^{salt}\right]}{\gamma_{cd,i}\left[C_{b,i}^{cd}\right]}\right) \tag{15}$$

Here, E_i° is the standard potential (V) of species i, $\gamma_{salt,i}$ is the activity coefficient of species i in the molten salt, $C_{b,i}^{salt}$ is the bulk concentration of species i in the molten salt (mol m^{-3}), and $\gamma_{cd,i}$ is the activity coefficient of species i in the liquid cadmium. The properties and thermodynamic data used in these equations are shown **Table 7**.

In the 2D model, we assumed that the concentration gradient exists only in the diffusion-dominant domain and that the bulk of the molten salt and cadmium pool were well-mixed, so that the concentration distribution is uniform throughout the bulk domain. Equations (16) and (17) are calculated to reflect the concentration changes in the bulk domain caused by the electrochemical reactions at the cathode and anode. The bulk concentration in the molten salt is changed by the both cathode and anode reactions as shown in the equation (16), whereas the bulk concentration of the cadmium anode is only changed by the anode reaction as shown in the equation (17).

$$V_{salt}\frac{dC_{b,i}^{salt}}{dt} = \oint^{anode}\left(\frac{i_{loc,i}}{n_i F}\right)dA + \oint^{cathode}\left(\frac{i_{loc,i}}{n_i F}\right)dA \tag{16}$$

$$V_{cd}\frac{dC_{b,i}^{cd}}{dt} = -\oint^{anode}\left(\frac{i_{loc,i}}{n_i F}\right)dA \tag{17}$$

Here, V_{salt} is the volume (m^3) of the molten salt region, V_{cd} is the volume (m^3) of liquid cadmium, and A is the area of the electrode (m^2).

ULSAN NATIONAL INSTITUTE OF SCIENCE AND TECHNOLOGY

Table 7. Electrochemical properties of U, Pu, and Nd in LiCl(59 mol%)-KCl(41 mol%) electrolyte and liquid Cd metal at 773K [22, 34].

Properties (unit)	Values
Standard potential of U (V vs. Cl_2/Cl^-)	-2.489
Standard potential of Pu (V vs. Cl_2/Cl^-)	-2.755
Standard potential of Nd (V vs. Cl_2/Cl^-)	-3.082
Activity coefficient of U in molten salt	1.697×10^{-3}
Activity coefficient of Pu in molten salt	9.793×10^{-3}
Activity coefficient of Nd in molten salt	3.508×10^{-4}
Activity coefficient of U in liquid Cd metal	88.7
Activity coefficient of Pu in liquid Cd metal	2.32×10^{-4}
Activity coefficient of Nd in liquid Cd metal	1.13×10^{-8}
Transfer coefficient for U	0.5
Transfer coefficient for Pu	0.5
Exchange current density for U (A cm^{-2})	5×10^{-4}
Exchange current density for Pu (A cm^{-2})	5×10^{-4}
Exchange current density for Nd (A cm^{-2})	5×10^{-4}

ULSAN NATIONAL INSTITUTE OF SCIENCE AND TECHNOLOGY

3.2. Numerical approach

The electrorefining model presented here was developed with the computational fluid dynamics software COMSOL 5.1 version, which is a multi-dimensional code that includes both fluid dynamics and electrochemistry. The 3D model was implemented using the secondary current distribution, transport of the diluted species, and rotating machinery with laminar flow modules. The 2D model was implemented using the secondary current distribution, transport of the diluted species, and boundary ordinary differential equations modules.

Figure 13 shows a numerical flow of the computational model. The 3D model combined the electrochemical reaction of the U species with the hydrodynamic calculation necessitated by a rotating cylinder electrode with sources and sinks at the electrodes. The 3D steady state model first solved the U concentration throughout the whole cell considering the deposition and dissolution reactions at the electrode surfaces and mass transport by diffusion and convection. By investigating the U concentration distribution using the 3D model, we provide a logically valid substitution for convection, using a constant diffusion layer thickness as the real value of the diffusion layer thickness in the 2D transient model.

Although the diffusion layer thicknesses of U, Pu, Nd molten salt, and liquid cadmium are different, most of the reactant at the cathode is U. Therefore, we used the diffusion layer thickness at the cathode calculated from the hydrodynamic properties of U obtained by 3D model. In addition, because we validated the assumed constant diffusion layer thickness, we used a constant diffusion layer thickness at the anode (0.002 cm) from previous literature [22]. Therefore, convection caused by hydrodynamic conditions was disregarded in the 2D model; we assumed a well-mixed state for the bulk region and considered only the mass concentration gradient in the diffusion-dominant domain. The 2D model focused on the competitive reactions among three species: U, Pu, and Nd.

The diffusion layer thickness was calculated as illustrated in **Figure 14**. First, the closest surface, which is 2.5×10^{-6} m from the cathode, was established and the average concentration of U at that surface was calculated. Next, the average concentration of U at the cathode was calculated, followed by the slope of the average concentration of U at the cathode and that at the closest surface to the cathode. Finally, we determined the point at which the slope of the U concentration intersected the bulk concentration, and this point was used as the diffusion layer thickness.

$$C_{bulk} = \frac{C_{avg}(x = 2.5 \times 10^{-6}\ m) - C_{avg}(x = 0)}{2.5 \times 10^{-6}\ m}\delta + C_{avg}(x = 0) \tag{18}$$

Here, C_{bulk} is the bulk concentration of U, x is the distance from the cathode surface; $C_{avg}(x=2.5\times10^{-6}\ m)$ is the average surface concentration of U at 2.5×10^{-6} m from the cathode, which

ULSAN NATIONAL INSTITUTE OF
SCIENCE AND TECHNOLOGY

was the nearest distance that could be calculated with our computational capacity; δ is the diffusion layer thickness; and $C_{avg}(x=0)$ is the average concentration of U at the cathode surface. The 3D model was calculated as a steady-state analysis. The 2D model was calculated as a transient analysis for 56.67 hours, and the result was compared to the ANL's experimental sampling results.

ULSAN NATIONAL INSTITUTE OF SCIENCE AND TECHNOLOGY

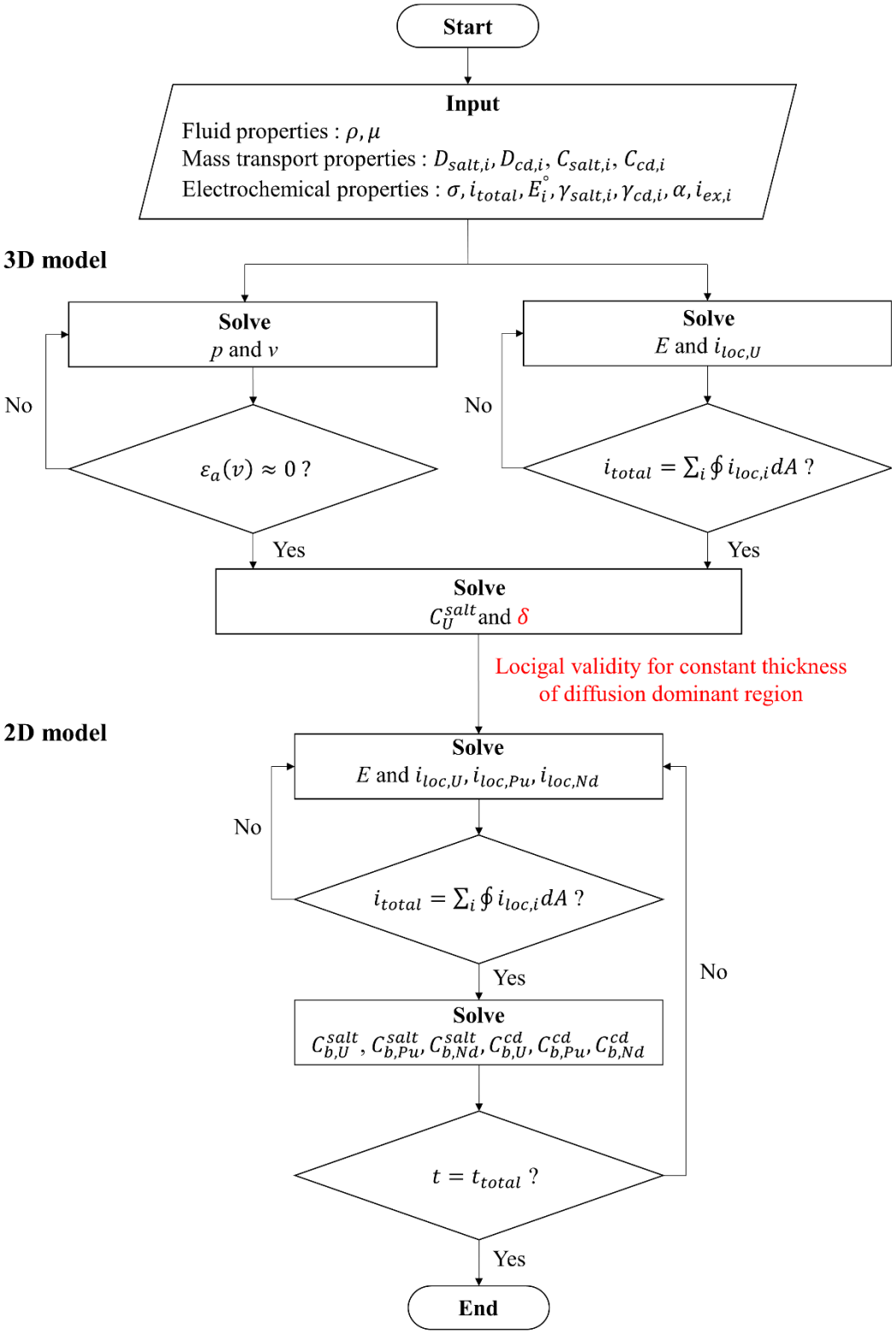

Figure 13. Numerical flow of the computational 3D steady state model and 2D transient model.

(ρ is the fluid density, μ is the dynamic viscosity, $D_{salt,i}$ is the diffusion coefficient of species i in the

ULSAN NATIONAL INSTITUTE OF SCIENCE AND TECHNOLOGY

molten salt, $D_{cd,i}$ is the diffusion coefficient of species i in the cadmium anode, $C_{salt,i}$ is the initial concentration of species i in the molten salt, $C_{cd,i}$ is the initial concentration of species i in the cadmium anode, σ is the electrolyte conductivity, i_{total} is the total applied current, E_i° is the standard potential of species i, $\gamma_{salt,i}$ is the activity coefficient of species i in the molten salt, $\gamma_{cd,i}$ is the activity coefficient of species i in the cadmium anode, α is the transfer coefficient, $i_{ex,i}$ is the exchange current density of species i, p is the pressure, v is the velocity, E is the electric potential, $i_{loc,i}$ is the local current density of species i, ε_a is the approximation error, $C_{b,i}^{salt}$ is the bulk concentration of species i in the molten salt, $C_{b,i}^{cd}$ is the bulk concentration of species i in the cadmium anode, t is the simulation time, and t_{total} is the total process time of the ANL experiment).

ULSAN NATIONAL INSTITUTE OF
SCIENCE AND TECHNOLOGY

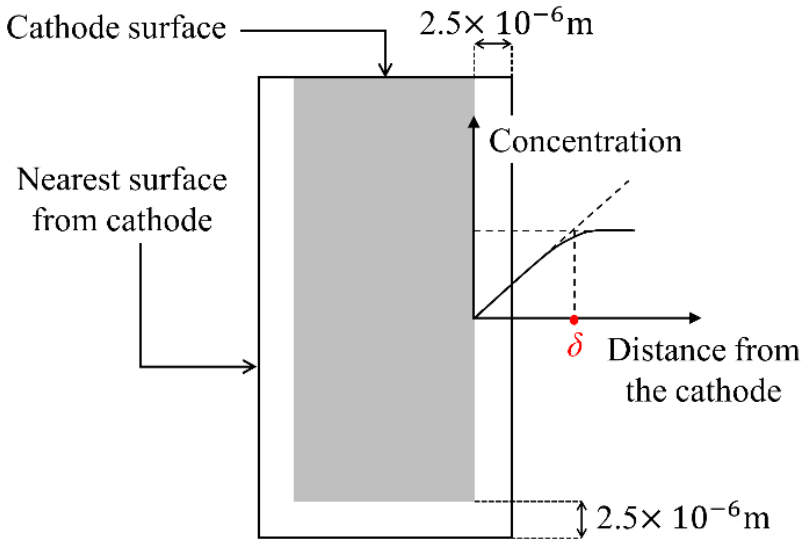

Figure 14. Schematic diagram of the diffusion layer thickness calculation (δ is the diffusion layer thickness).

ULSAN NATIONAL INSTITUTE OF
SCIENCE AND TECHNOLOGY

Figure 15 shows the design and mesh configuration of the 3D hydrodynamic model of the electrorefining cell, where we assumed a cell consisting of a simple rotating solid cylinder electrode, which is dominant in hydrodynamic effects, instead of modeling the full complexity of the ANL electrorefining cell configuration. Only the interface between each electrode and the molten salt was considered, and not the volume of each electrode, because the electrochemical reactions occur at the electrode surfaces and the ion behavior in the molten LiCl-KCl eutectic salt was the main focus of this investigation.

In **Figure 15**. **(**a), the smaller cylinder at the center of the top is the cathode surface, where the reduction reaction occurs. The cathode-molten salt interface occurs across the surface area of the cylinder, which has a 1.6 cm radius and a height of 7.5 cm. The bottom of the cell is the anode surface, where the oxidation reaction occurs. The radius of the anode surface is 7.6 cm. **Figure 15**. (b) shows the mesh configuration of the 3D model. Because the reaction occurs at the electrode surfaces, finer meshes were established in the vicinity of the electrodes and relatively coarser meshes were established for the bulk region. In the vicinity of the electrode, three layers of mesh were constructed in the distance within 2.5×10^{-6} m of the electrode surface, and 10 layers of mesh were constructed in the distance within 5×10^{-5} m of the electrode surface from the electrodes.

Figure 16 shows the design and mesh configuration of the 2D model, which is a cross section in the *yz*-plane of the 3D model at x = 0. The perpendicular and bottom lines shown in blue in **Figure 16** are the cathode and anode surfaces, respectively. The right side pictures in **Figure 16** shows the mesh configuration in the vicinity of the cathode and anode surfaces, respectively. The 10 layers were built in the diffusion-dominant domain. Two diffusion layers were established in the vicinity of the interface between the molten salt and cadmium anode. One of these layers is the diffusion-dominant domain of the molten salt side of the anode above the interface, and the other is that of the liquid cadmium side of the anode below the interface. The total numbers of meshes were 319,152 for the 3D model and 25,195 for the 2D model.

ULSAN NATIONAL INSTITUTE OF SCIENCE AND TECHNOLOGY

(a)

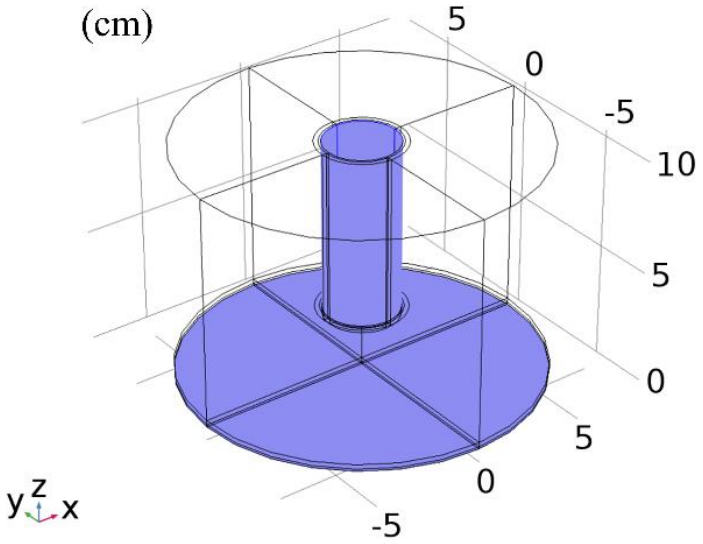

(b)

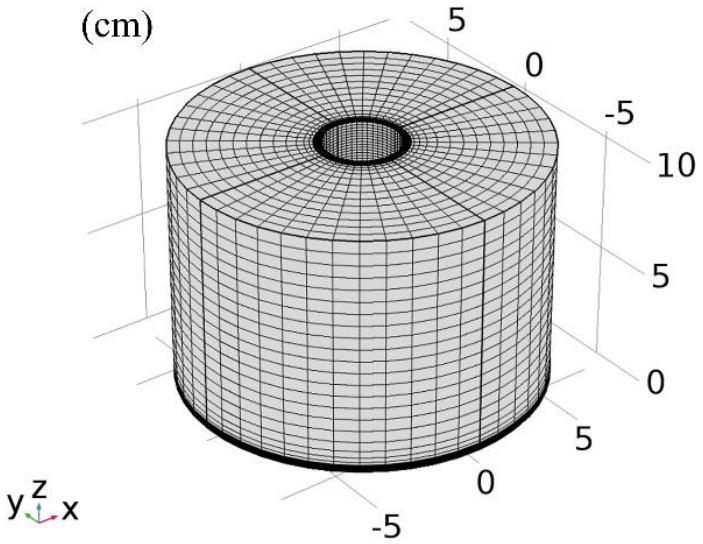

Figure 15. 3D computational domains of (a) electrorefining cell with rotating solid cylinder cathode (the small cylinder at the center of the cell is the cathode surface, and the circle at the bottom of the cell is the anode surface) and (b) mesh configuration of whole cell (all dimensions in cm).

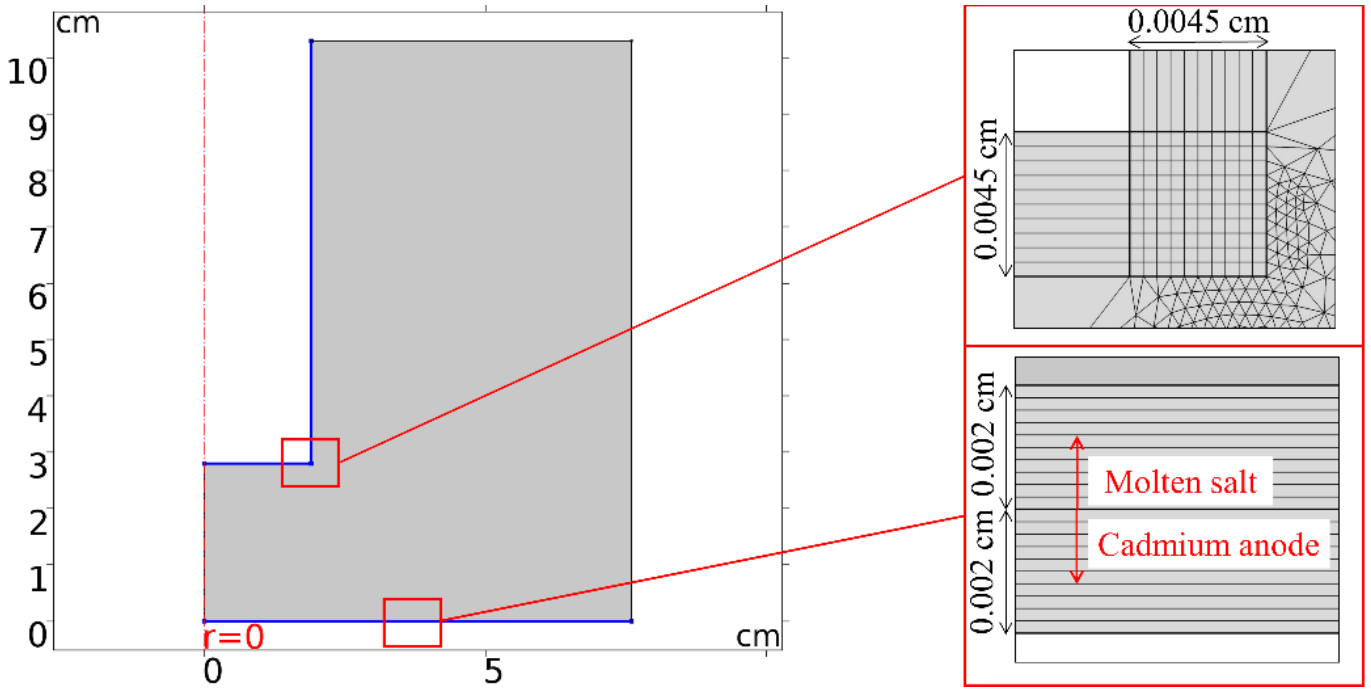

Figure 16. 2D computational domains of the Argonne National Laboratory electrorefining cell with enlarged picture of diffusion dominant domain in the vicinity of the cathode and anode. The picture of the upper side at the right is the vicinity of the cathode and that of the lower side is the vicinity of anode.

ULSAN NATIONAL INSTITUTE OF SCIENCE AND TECHNOLOGY

ULSAN NATIONAL INSTITUTE OF
SCIENCE AND TECHNOLOGY

IV. 3D Steady-state Profiles of Momentum and Mass Transfer

4.1 Velocity and concentration distribution

Figure 17. (a) shows the velocity magnitude for U ions in the electrochemical cell. This model used U ion as representative ions to determine the regions where diffusion is the dominant mass transfer mechanism for electrochemical reactions. The cathode rotated at a speed of 35 rpm counterclockwise from the top. The direction of the velocity field is expressed in **Figure 17**. (b), where the lengths of the arrows indicate the magnitude. By applying no slip at the wall, the greatest magnitude reached 0.05864 m/s at the side surface of the cathode. The magnitude at the bulk electrolyte varied from 0.001 to 0.01 m/s. The velocity field was well-developed in the top region of the electrorefiner, where the free surface condition was applied. At the bottom of the cathode, an upward helical flow developed from the anode to the cathode, which is typically observed with rotating cylinder electrodes [37].

Figure 18. (a) shows the contours of U ion concentrations in the molten salt in relation to the *yz*-cross section of the cell. Although the concentration of U ions remained almost constant in the bulk region, the concentration changed significantly near the surfaces of both electrodes and in the region between the bottom of the cathode to the anode surface. **Figure 18**. (b) shows the concentration profile along a line from the center of the anode surface to the center of the cathode's bottom surface. The point x = 0 indicates the anode surface, and x = 2.8 indicates the cathode surface. Although convection was dominant in the bulk electrolyte, diffusion became dominant near the surface of the cathode.

As expected, the concentration of U ions decreased in the vicinity of the cathode surface, developing a diffusion boundary layer up to several tens of micrometers. In contrast, in the vicinity of the anode, a diffusion-dominant region was hard to define because a concentration gradient formed not only near the surface of the anode but also distant from the surface of the anode.

Figure 18. (c) shows the concentration of U at the *xy*-cross section where z = 2.8 cm, the location of the bottom surface of the cathode. The concentration of U at the bottom surface, small circle at the center, was much lower than other bulk regions because of the reduction reactions from U ions to U metal. In connection with our previous observation of a thin diffusion layer at the cathode from **Figure 18**. (b), the gradient of the concentration of U was very steep near the circumferential surface of the cathode. This concentration distribution is caused by the convection induced by the rotating solid cylinder electrode.

The velocity of U was the highest at the circumference of the cathode, whereas the velocity of U was the lowest at the center of the cathode bottom surface and near the circumference of the cell (**Figure 18**. (d)). The convection effect in those regions was insignificant. These conditions affected the concentration and velocity of U at the anode surface as well (**Figure 18**. (e)-(f)). The velocity in those

ULSAN NATIONAL INSTITUTE OF
SCIENCE AND TECHNOLOGY

regions was much smaller than in other regions, and the concentration was much larger in those regions with smaller velocities. In addition, the order of the velocity of U at the cathode surface was 10^{-2} m/s and that of U at the anode surface was 10^{-6} m/s. Therefore, the convection was much more active near the cathode and a very steep concentration gradient appeared, as did the thin diffusion layer near the cathode. In contrast, the convection was inactive near the anode surface and the concentration gradient there was gradual.

ULSAN NATIONAL INSTITUTE OF
SCIENCE AND TECHNOLOGY

(a)

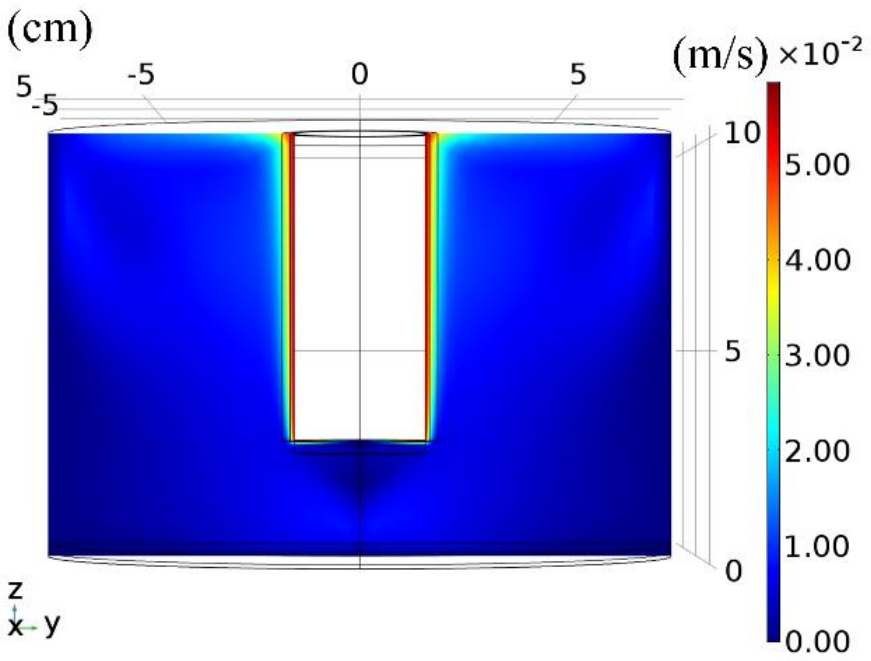

(b)

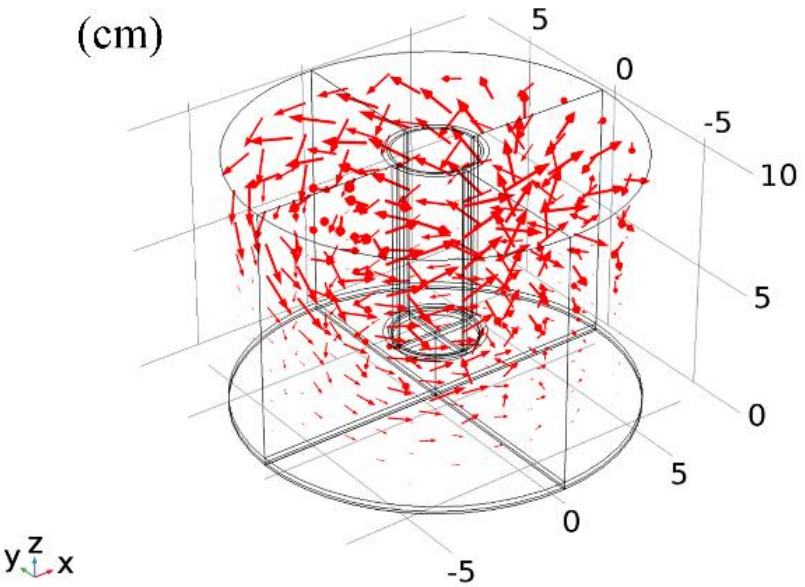

Figure 17. (a) Velocity (m/s) of U in molten salt at the *yz*-cross section of 3D hydrodynamic model analyzing a rotating cylinder solid electrode. (b) Arrows indicate the direction and magnitude of velocity of U in molten salt.

ULSAN NATIONAL INSTITUTE OF SCIENCE AND TECHNOLOGY

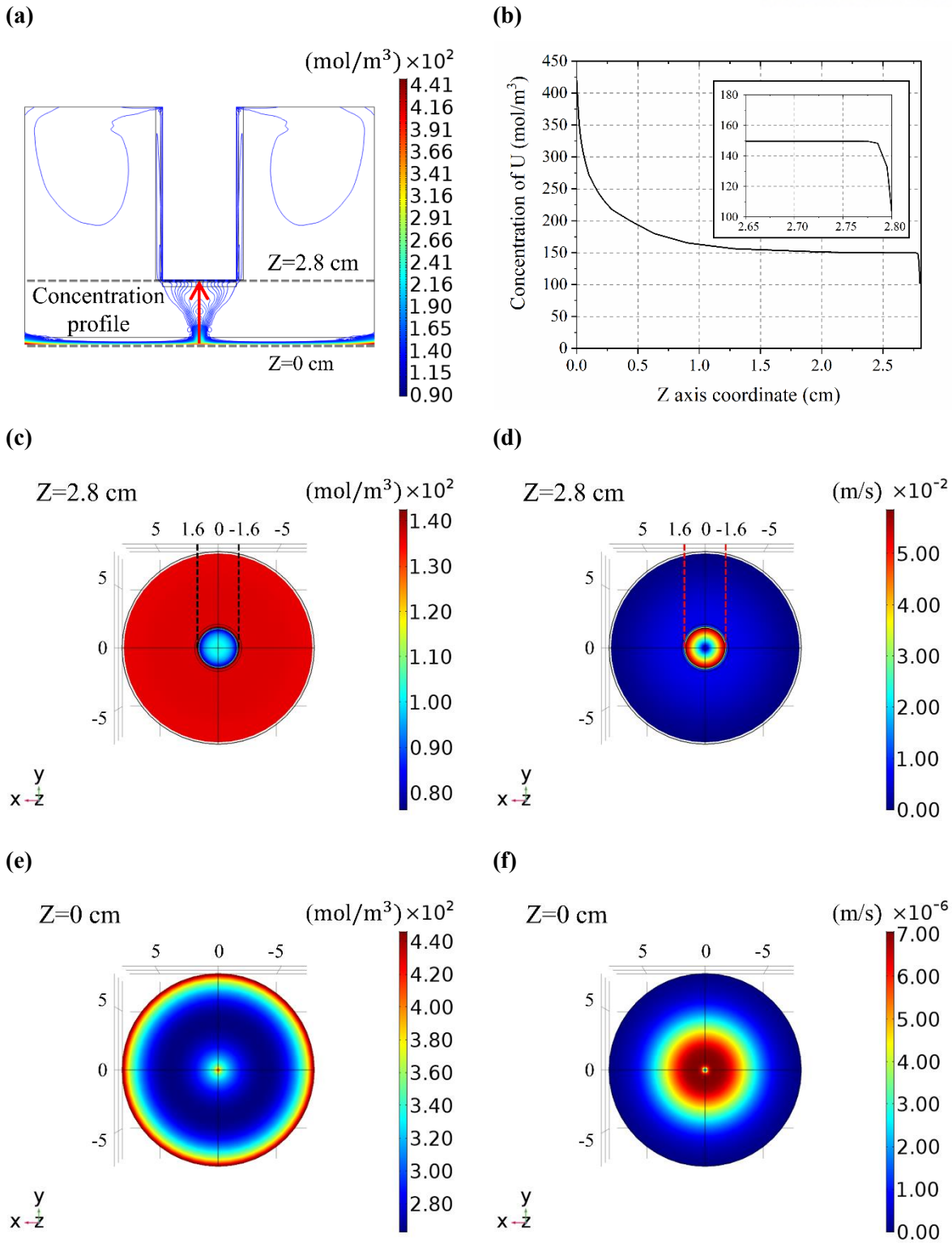

Figure 18. (a) Contours of U concentration in molten salt at the *yz*-cross section. (b) U concentration profile along the line from the center of the anode surface to the center of the cathode bottom surface. (c) Concentration of U in molten salt at the *xy*-cross section where z = 2.8 cm, the location of the cathode's bottom surface (The smaller circle at the center with a radius of 1.6 cm is the cathode's bottom surface and the other region is the cross section of the electrolyte). (d) Velocity of U in molten salt at

ULSAN NATIONAL INSTITUTE OF
SCIENCE AND TECHNOLOGY

the *xy*-cross section where z = 2.8 cm, the location of the cathode's bottom surface (The smaller circle at the center with a radius of 1.6 cm is the cathode's bottom surface and the other region is the cross section of the electrolyte). (e) Concentration of U in molten salt at the *xy*-cross section where z = 0 cm, the location of the anode surface. (f) Velocity of U in molten salt at the *xy*-cross section where z = 0 cm, the location of the anode surface.

ULSAN NATIONAL INSTITUTE OF
SCIENCE AND TECHNOLOGY

4.2 Thickness of diffusion-dominant regions

The thickness of diffusion-dominant regions from the surface of the cathode was calculated using equation (14). We investigated diffusion-dominant regions rather than a constant diffusion boundary layers because the actual thickness of a diffusion boundary layer changes throughout the electrorefining process for all species. The thickness of diffusion-dominant regions was determined to be reasonably large, reflecting actual surface kinetics and still reducing the computational resources required in the 2D electrochemical model.

The gradient of the average concentration was obtained from the difference in average concentrations at the surface of the cathode and the surface nearest to the cathode. The calculated thickness of diffusion dominant regions at the cathode was $4.5 \times 10^{-5} \pm 1.3\%$ m using average concentration distributions from the surface of the cathode. These results support the assumptions in the 2D electrochemical reaction model, namely, that the concentration distribution is uniform in the bulk electrolyte and that diffusion is the dominant mass transfer mechanism near the cathode.

Although the result of the 3D model provided a logical validation for assuming a constant diffusion layer for the cathode and not for the anode, the ANL experiment used an agitator with three blades, one each in the molten salt region, at the interface between the molten salt and cadmium anode, and in the cadmium anode region; these blades impart an active convection effect to the anode surface and thus the same logical validity can apply to the anode as well. We used the constant thickness of 0.002 cm for the diffusion dominant regions, from the literature [22].

The results were obtained at steady state because the same amount of U was dissolved from the anode and deposited on the cathode in the 3D hydrodynamic model. Using the thickness of diffusion dominant regions is a conservative approach because the single species satisfies all necessary charge conservation principles.

ULSAN NATIONAL INSTITUTE OF
SCIENCE AND TECHNOLOGY

V. Benchmark of U-Pu-Nd Electrochemical Reactions using 2D Kinetic Model

5.1 Anodic dissolution

Figure 19. (a) shows the results of competitive anodic dissolution of U, Pu, and Nd. Although U was initially a major source of anodic current, U, Pu, and Nd started to dissolve from the liquid Cd metal to the molten salt together from the beginning. Although the standard potential of Pu is more negative than that of U, the initial dissolution rate of U was much faster. The difference was caused by the much larger activity coefficient (~88) of U in liquid Cd metal than that (~ 2.32×10^{-4}) of Pu. At 500 ℃, Pu forms intermetallic compounds with Cd, whereas U does not above 723 K [38, 39]. The Nd in the cadmium anode was almost exhausted after 10 hours, and the concentration converged to zero after that time.

From the Nernst equation, equation (15), the equilibrium potentials of U, Pu, and Nd at the anode were calculated as presented in **Figure 20.** (a). Although the equilibrium potential of Nd was more negative than that of U, the limiting current of Nd could not satisfy the total current because of the low concentration in the cadmium anode, and therefore the current of U was much bigger than that of Nd (**Figure 20.** (c)). The equilibrium potential of U was more negative than that of Pu during most of the simulation time. Overall, the potentials of both U and Pu continuously increased as they were dissolved from liquid Cd metal. The potential gap between U and Pu was gradually reduced, and the rate became more rapid after 50 hours, when U in liquid Cd metal was almost exhausted. As a result, the current of Pu became greater than that of U after approximately 48 hours of operating time, as shown in **Figure 20.** (c).

Figure 21. (a) shows the local current density of those species along a line of the anode surface. At the center of the anode surface, the values were lowest. Because of the low convection effect, the oxidized species were concentrated at the center of anode in the molten salt side, the metals were hard to be oxidized from the cadmium anode.

ULSAN NATIONAL INSTITUTE OF
SCIENCE AND TECHNOLOGY

5.2 Cathode deposition

As shown in **Figure 19**. (b), U was the only species deposited on the surface of the cathode for nearly 50 hours. After U ions were exhausted in the bulk electrolyte, Pu started to be co-deposited on the cathode. **Figure 20.** (b) shows the variation of the equilibrium potentials. The overpotential of U was negative and the sign of the exponent of local current density was positive during all of simulation time. Therefore, U ions occupied most of the cathodic current during most of the process. The overpotential of Pu was positive, and therefore the sign of the exponent of local current density was negative up to 50 hours. However, the sign of the exponents of Pu reversed at approximately 50 hours, when the cathodic current of Pu increased steeply and that of U decreased, and the magnitude of cathodic current of Pu exceed that of U at approximately 53 hours (**Figure 20.** (d)). During the whole simulation, the cathodic current of Nd was low enough to be treated as negligible. On-set of Pu deposition around 50 hours is successfully estimated at correct time to catch up the rapid increase of deposition rate of Pu at the solid electrode.

Figure 21. (b) shows the local current density of those species along a line of the cathode surface. The highest values were found in the edge of the cathode surface. It is because the highest velocity was formed at the edge of the cathode and therefore the reactants were actively supplied from the bulk region.

ULSAN NATIONAL INSTITUTE OF
SCIENCE AND TECHNOLOGY

5.3 Bulk concentration of the molten salt

The change in the bulk concentration can be interpreted as the summation of cathode depletion and anode dissolution reactions. At the cathode, only U satisfied the total reduction current. At the anode, the total anodic current was split by U, Pu, and Nd (**Figure 20.** (c), (d)). Thus, the concentration of U in the molten salt continuously decreased and that of Pu increased until approximately 53 hours of operating time as shown in **Figure 19.** (c). As the concentration of U in the molten salt and cadmium decreased, the limiting current of U could not fully satisfy the total cathodic and anodic current.

Finally, the cathodic and anodic current of U simultaneously decreased and the bulk concentration of U remained constant. Likewise, the cathodic and anodic current of Pu simultaneously increased and the bulk concentration of Pu remained constant. The model successfully predicts varying rates of concentration changes of U and Pu at the end of simulation. However, the Nd was dissolved from the cadmium anode in early reactions, and there was almost no reduction reaction at the cathode throughout the whole simulation time. Therefore, the bulk concentration of Nd in the molten salt increased until 10 hours and then remained constant.

ULSAN NATIONAL INSTITUTE OF SCIENCE AND TECHNOLOGY

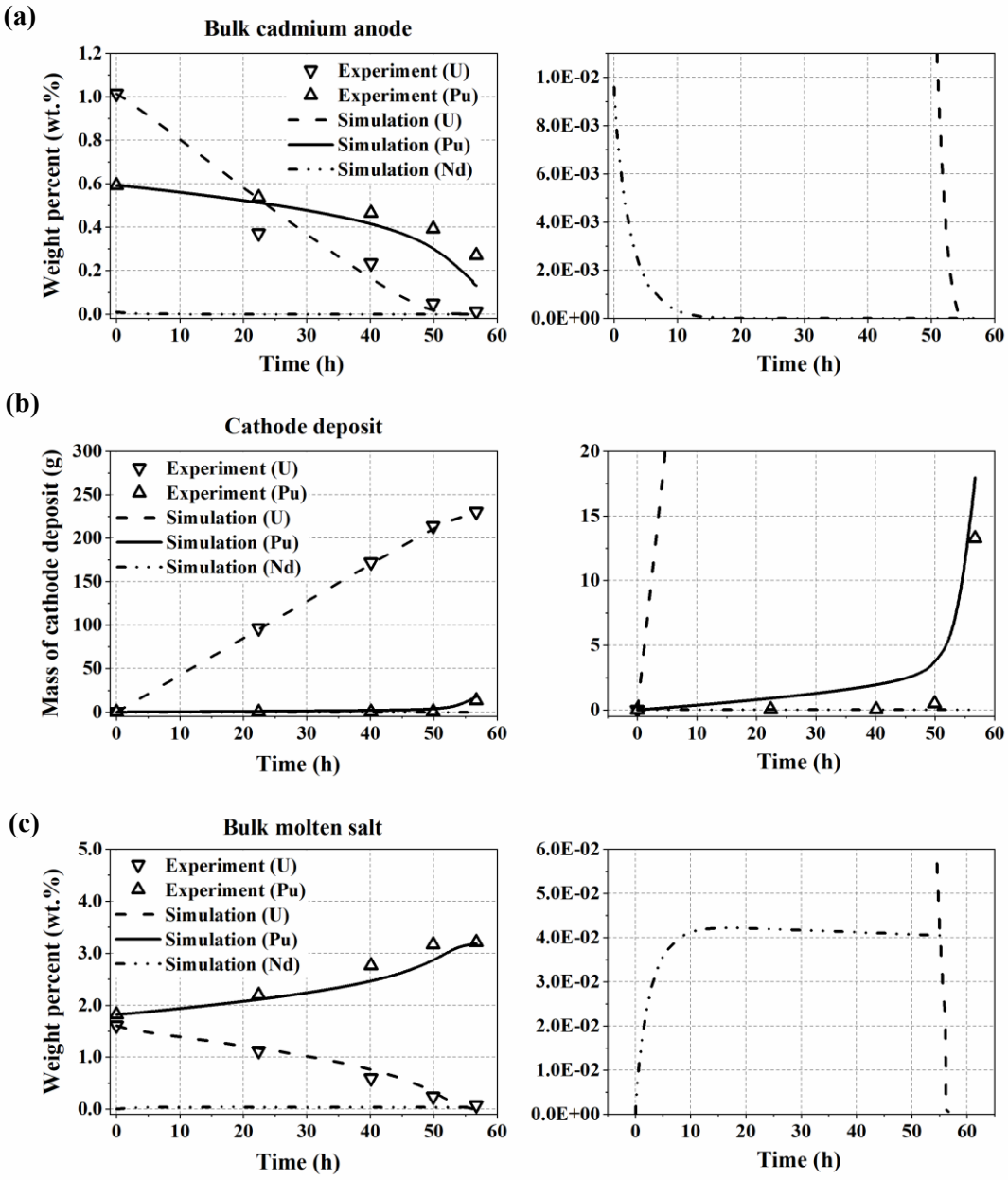

Figure 19. (a) Weight percent of U, Pu, and Nd in bulk of the cadmium anode. (b) Amount of metal deposition on the cathode. (c) Weight percent of U, Pu, and Nd in bulk of the molten salt. The initial amount of Nd in the cadmium anode was 9.6×10^{-3} wt%, which is smaller than the detection limit. Therefore, the amounts of Nd in the molten salt, cadmium anode, and metal deposition were very low, as shown in the enlarged picture for Nd at right.

ULSAN NATIONAL INSTITUTE OF
SCIENCE AND TECHNOLOGY

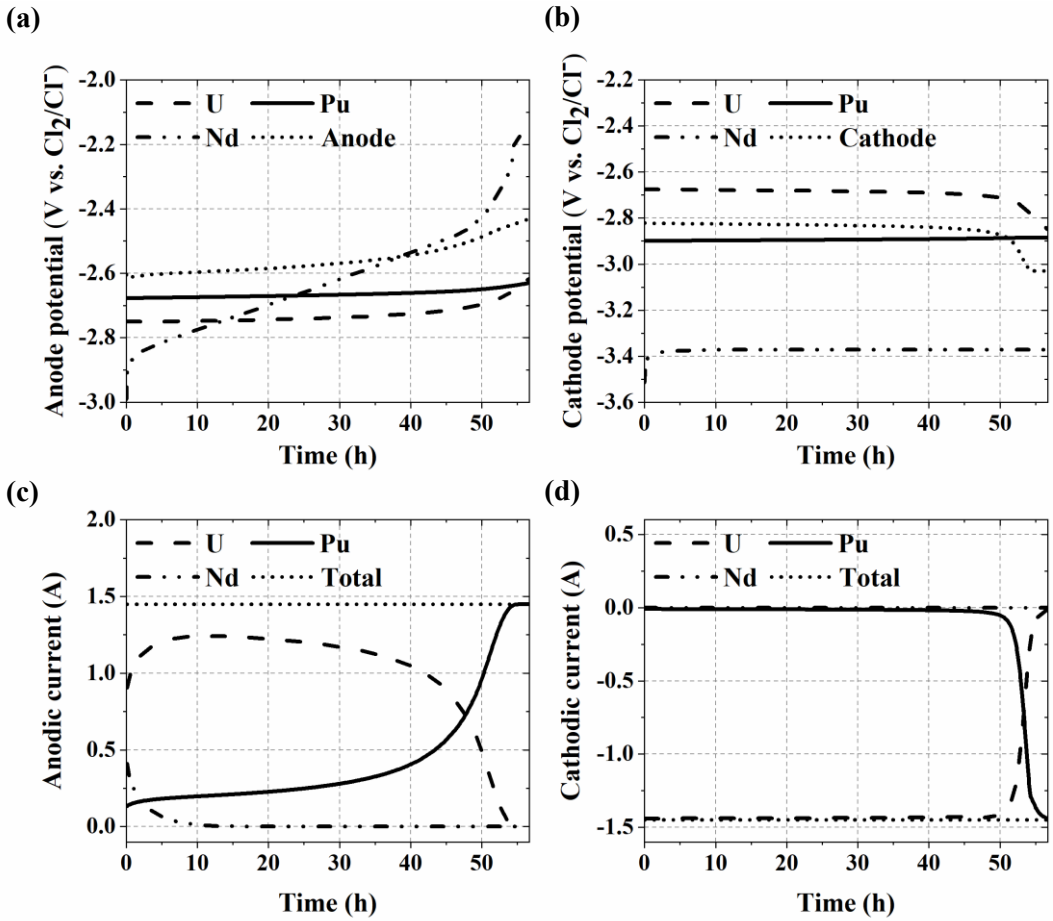

Figure 20. (a) Anode equilibrium potential of U, Pu, and Nd with anode potential. (b) Cathode equilibrium potential of U, Pu, and Nd with cathode potential. (c) Anodic current of U, Pu, and Nd with total anodic current. (d) Cathodic current of U, Pu, and Nd with total cathodic current.

ULSAN NATIONAL INSTITUTE OF SCIENCE AND TECHNOLOGY

(a)

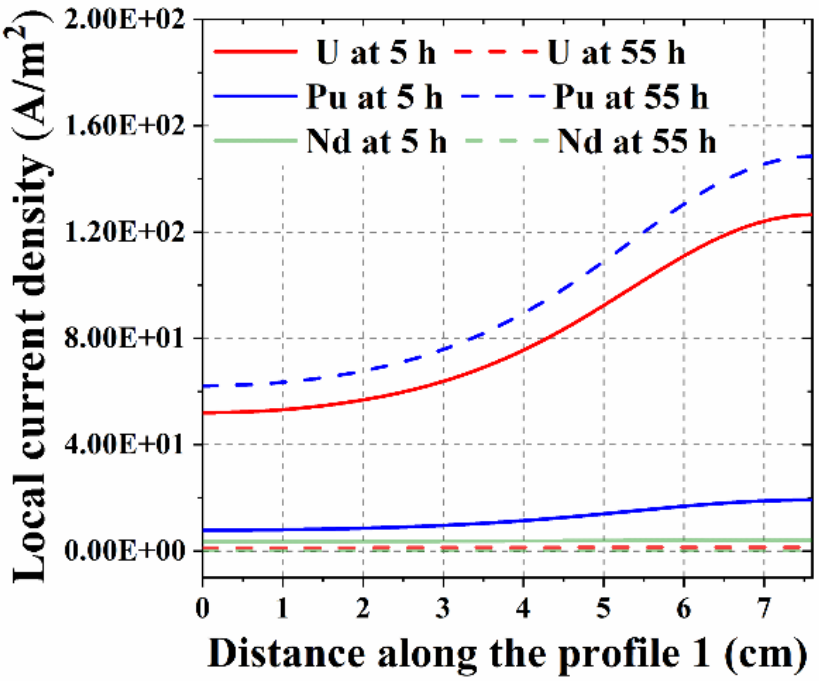

(b)

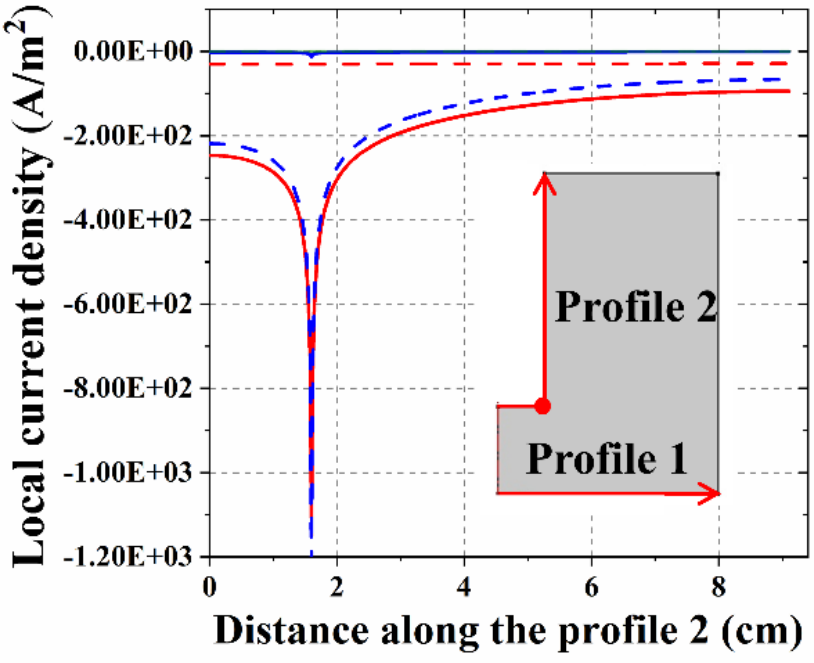

Figure 21. (a) Local current density of U, Pu, and Nd along the profile 1 (a line from the center of the anode to the edge). (b) Local current density of U, Pu, and Nd along the profile 2 (a line from the center of the cathode bottom to the top of the cathode side).

ULSAN NATIONAL INSTITUTE OF
SCIENCE AND TECHNOLOGY

5.4 Sources of disparities between the model and experiment

The overall tendency of the modeling and experimental results were well-matched. In particular, the amount of metal deposition at the cathode matched perfectly. However, discrepancies between the modeling and experimental results include the concentrations of U and Pu at the cadmium anode and molten salt, and the presence of unspecified amounts of other species such as Ce, Y, Nd.

To analyze the causes, we compared the total amount of metal deposition at the cathode and that of dissolution from the cadmium anode. The total weight of U metal deposited was 230.37 g (0.9678 mol), and that of Pu was 13.26 g (0.05434 mol). The total dissolution weight of U was 165.33 g (0.6946 mol), and that of Pu was 53.13 g (0.2177 mol). There was a 0.1098 mol difference in the quantities that participated in the reduction and oxidation reactions.

This difference violates the charge conservation law, and thus we assumed that other species may have dissolved from the cadmium anode to the molten salt in the amount of the difference. We selected Nd as a representative of the lanthanide species and added 0.1098 mol of Nd into the cadmium anode. After the addition of Nd, the modeling and experimental concentrations at the cadmium anode were very well-matched (**Figure 22.** (a)) and the amount of metal deposition still matched well (**Figure 22.** (b)). However, the discrepancy in the bulk concentration of U and Pu in the molten salt worsened (**Figure 22.** (c)), indicating that some experimental errors like nonhomogeneous sampling, human errors must have occurred in the molten salt or cadmium anode.

ULSAN NATIONAL INSTITUTE OF SCIENCE AND TECHNOLOGY

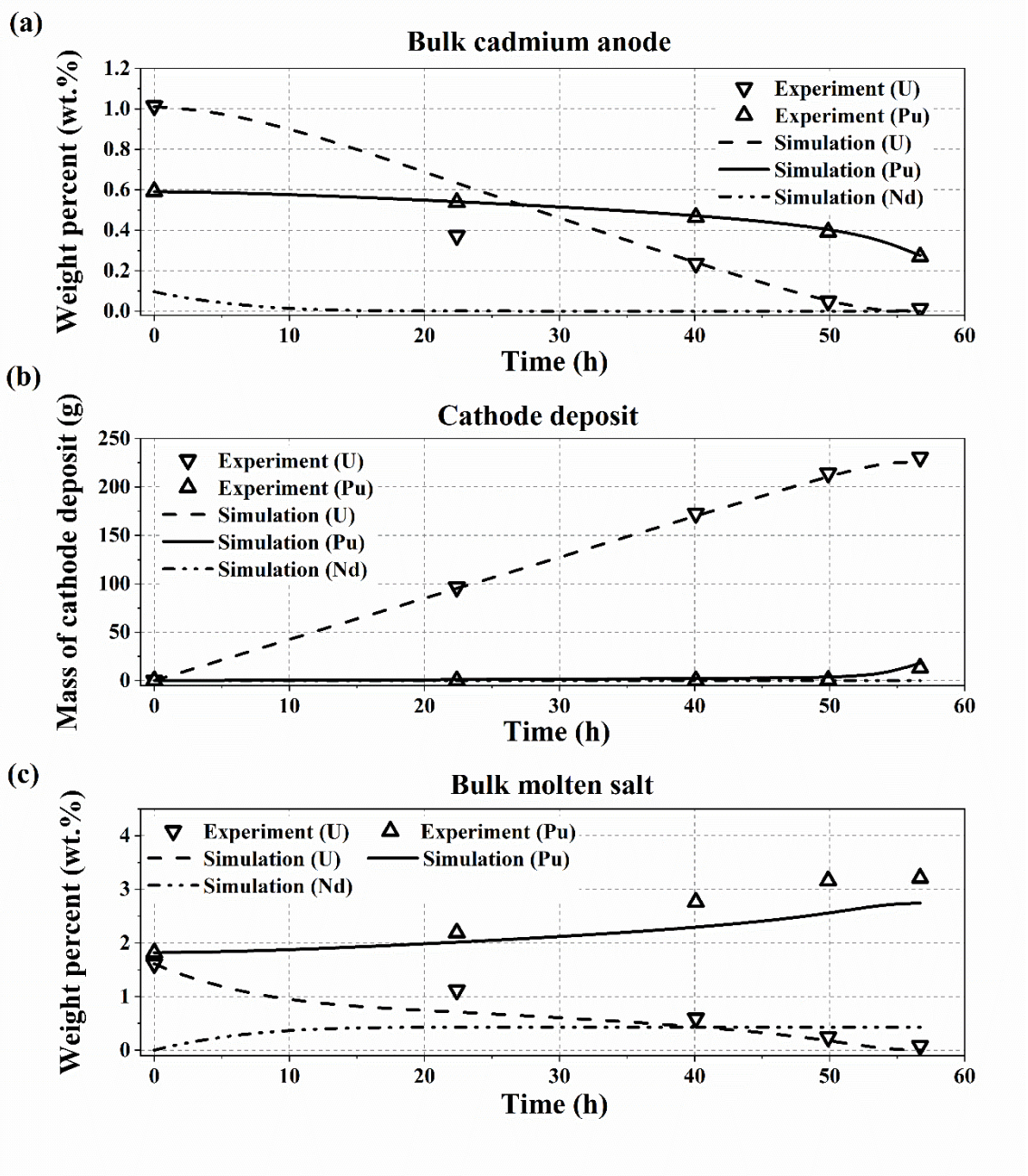

Figure 22. (a) Weight percent of U and Pu in bulk of the cadmium anode. (b) Amount of metal deposition on the cathode. (c) Weight percent of U and Pu in bulk of the molten salt. The difference between the cathode deposition and anode dissolution of Nd, 0.1098 mol, was added to the cadmium anode.

ULSAN NATIONAL INSTITUTE OF
SCIENCE AND TECHNOLOGY

VI. Conclusions

Liquid metal electrodes and rotating cylinder solid electrodes are widely used in research and industry applications. In this paper, computational coupling of electrochemistry and fluid mechanics is developed in 3D and 2D models for multiple components across multi-phases at the same time. This study develops a computational model combining a 3D model for calculating single-species mass transport under rotating solid cylinder electrode and a 2D model for calculating multi-species electrochemical reactions.

The velocity field, concentration distribution, and diffusion layer thickness were calculated with the 3D model. These 3D results validated the assumption of a constant thickness of the diffusion-dominant region, and the calculated thickness was applied to a 2D multispecies model to investigate the equilibrium potential of U, Pu, and Nd at both electrodes, cathodic and anodic current, and bulk concentration of U, Pu, and Nd in the molten salt and cadmium anode. The computational model is validated against lab-scale experimental data using a rotating cylinder solid metal cathode and liquid cadmium anode in the Argonne National Laboratory. The simulated and experimental results showed good agreement in not only the bulk concentration in the molten salt and cadmium anode but also the metal deposits on the solid cathode.

Later, I will expand the analysis target in this model to the whole species in the used nuclear fuel and develop 3D fully-coupled electrorefining model with parallel computing system. In addition, more realistic hydrodynamic conditions will be considered in the computational model by including effects of the agitator.

ULSAN NATIONAL INSTITUTE OF
SCIENCE AND TECHNOLOGY

REFERENCES

[1] H.-S. Lee, G.-I. Park, K.-H. Kang, J.-M. Hur, J.-G. Kim, D.-H. Ahn, Y.-Z. Cho, E.-H. Kim, Pyroprocessing technology development at KAERI, Nuclear Engineering and Technology, 43 (2011) 317-328.

[2] H. Ju, I. Hahm, S. Sohn, I.S. Hwang, Long-term Environmental Assessment of Waste from PyroGreen System, Procedia Chemistry, 21 (2016) 425-432.

[3] O.R.N. Laboratory, ORNL DWG 92A-242.

[4] O.R.N. Laboratory, ORNL DWG 95A-534.

[5] N.R. Council, Nuclear Wastes : Technologies for Separations and Transmutation, National Academy Press, (1996).

[6] H. LEE, G.-I. PARK, K.-H. KANG, J.-M. HUR, J.-G. KIM, D.-H. AHN, Y.-Z. CHO, E.H. KIM, PYROPROCESSING TECHNOLOGY DEVELOPMENT AT KAERI, NUCLEAR ENGINEERING AND TECHNOLOGY, VOL 43 (2011).

[7] J.J. Laidler, J.E. Battles, W.E. Miller, E.C. Gay, DEVELOPMENT OF IFR PYROPROCESSING TECHNOLOGY, GLOBAL 1993, (1993).

[8] B.L. Ellis, L.F. Nazar, Sodium and sodium-ion energy storage batteries, Current Opinion in Solid State and Materials Science, 16 (2012) 168-177.

[9] Z. Yang, J. Zhang, M.C.W. Kintner-Meyer, X. Lu, D. Choi, J.P. Lemmon, J. Liu, Electrochemical Energy Storage for Green Grid, Chemical Reviews, 111 (2011) 3577-3613.

[10] H. Kim, D.A. Boysen, J.M. Newhouse, B.L. Spatocco, B. Chung, P.J. Burke, D.J. Bradwell, K. Jiang, A.A. Tomaszowska, K. Wang, W. Wei, L.A. Ortiz, S.A. Barriga, S.M. Poizeau, D.R. Sadoway, Liquid Metal Batteries: Past, Present, and Future, Chemical Reviews, 113 (2013) 2075-2099.

[11] Y. Castrillejo, M.R. Bermejo, P.D. Arocas, A.M. Martínez, E. Barrado, The electrochemical behaviour of the Pr(III)/Pr redox system at Bi and Cd liquid electrodes in molten eutectic LiCl–KCl, Journal of Electroanalytical Chemistry, 579 (2005) 343-358.

[12] S.X. Li, S.D. Herrmann, K.M. Goff, M.F. Simpson, R.W. Benedict, Actinide Recovery Experiments with Bench-Scale Liquid Cadmium Cathode in Real Fission Product-Laden Molten Salt, Nuclear Technology, 165 (2009) 190-199.

[13] D. Vaden, S.X. Li, B.R. Westphal, K.B. Davies, T.A. Johnson, D.M. Pace, Engineering-Scale Liquid Cadmium Cathode Experiments, Nuclear Technology, 162 (2008) 124-128.

[14] S. Seo, S. Choi, B.G. Park, Transient modeling of spent nuclear fuel electrorefining with liquid metal electrode, Journal of Nuclear Materials, 491 (2017) 115-125.

[15] V.M. Volgin, A.D. Davydov, Effect of migration on homogeneous redox electrocatalysis at rotating disk electrode, Electrochimica Acta, 259 (2018) 56-65.

ULSAN NATIONAL INSTITUTE OF SCIENCE AND TECHNOLOGY

[16] J. Park, S. Choi, R. Hoover, K.-R. Kim, S. Sohn, Y.-H. Shin, S. Phongikaroon, M. Simpson, I.S. Hwang, Comparison between Numerical Simulations and Experimental Results on Copper Deposition in Rotating Cylinder Hull Cell, Electrochimica Acta, 164 (2015) 218-226.

[17] C.T.J. Low, E.P.L. Roberts, F.C. Walsh, Numerical simulation of the current, potential and concentration distributions along the cathode of a rotating cylinder Hull cell, Electrochimica Acta, 52 (2007) 3831-3840.

[18] M. Rosales, T. Pérez, J.L. Nava, Computational fluid dynamic simulations of turbulent flow in a rotating cylinder electrode reactor in continuous mode of operation, Electrochimica Acta, 194 (2016) 338-345.

[19] I. Johnson, The thermodynamics of pyrochemical processes for liquid metal reactor fuel cycles, Journal of Nuclear Materials, 154 (1988) 169-180.

[20] H.P. Nawada, N.P. Bhat, Thermochemical modelling of electrotransport of uranium and plutonium in an electrorefiner, Nuclear Engineering and Design, 179 (1998) 75-99.

[21] S. Ghosh, B.P. Reddy, K. Nagarajan, P.R.V. Rao, PRAGAMAN: A Computer Code for Simulation of Electrotransport during Molten Salt Electrorefining, Nuclear Technology, 170 (2010) 430-443.

[22] T. Kobayashi, M. Tokiwai, Development of TRAIL, a simulation code for the molten salt electrorefining of spent nuclear fuel, Journal of alloys and compounds, 197 (1993) 7-16.

[23] R.O. Hoover, S. Phongikaroon, M.F. Simpson, S.X. Li, T.-S. Yoo, Development of Computational Models for the Mark-IV Electrorefiner—Effect of Uranium, Plutonium, and Zirconium Dissolution at the Fuel Basket-Salt Interface, Nuclear Technology, 171 (2010) 276-284.

[24] J. Zhang, Kinetic model for electrorefining, part I: Model development and validation, Progress in Nuclear Energy, 70 (2014) 279-286.

[25] B. Krishna Srihari, S. Agarwal, B. Prabhakara Reddy, P. Satya Sai, B. Muralidharan, K. Nagarajan, Modeling the Molten Salt Electrorefining Process for Spent Metal Fuel Using COMSOL, Separation Science and Technology, 50 (2015) 2276-2283.

[26] Z. Tomczuk, J.P. Ackerman, R.D. Wolson, W.E. Miller, Uranium Transport to Solid Electrodes in Pyrochemical Reprocessing of Nuclear Fuel, Journal of The Electrochemical Society, 139 (1992) 3523-3528.

[27] R.M. Cumberland, M.-S. Yim, Development of a 1D transient electrorefiner model for pyroprocess simulation, Annals of Nuclear Energy, 71 (2014) 52-59.

[28] S. Choi, J. Park, K.-R. Kim, H. Jung, I. Hwang, B. Park, K. Yi, H.-S. Lee, D. Ahn, S. Paek, Three-dimensional multispecies current density simulation of molten-salt electrorefining, Journal of Alloys and Compounds, 503 (2010) 177-185.

[29] S. Choi, J. Park, R.O. Hoover, S. Phongikaroon, M.F. Simpson, K.-R. Kim, I.S. Hwang, Uncertainty studies of real anode surface area in computational analysis for molten salt electrorefining, Journal of Nuclear materials, 416 (2011) 318-326.

ULSAN NATIONAL INSTITUTE OF SCIENCE AND TECHNOLOGY

[30] K. Kim, S. Choi, D. Ahn, S. Paek, H. Lee, I. Hwang, Electro-fluid analysis of a molten-salt electrorefiner with rotating cruciform anode baskets, Journal of radioanalytical and nuclear chemistry, 286 (2010) 801-806.

[31] J. Li, D. Mcnelis, M.-s. Yim, A comprehensive electrorefining process simulation model for pyroprocessing of spent fuel, (2011).

[32] K.R. Kim, S.Y. Choi, D.H. Ahn, S. Paek, B.G. Park, H.S. Lee, K.W. Yi, I.S. Hwang, Computational analysis of a molten-salt electrochemical system for nuclear waste treatment, Journal of Radioanalytical and Nuclear Chemistry, 282 (2009) 449.

[33] J. Bae, H.O. Nam, K.W. Yi, B.G. Park, I.S. Hwang, Numerical assessment of pyrochemical process performance for PEACER system, Nuclear Engineering and Design, 240 (2010) 1679-1687.

[34] J. Zhang, Electrochemistry of actinides and fission products in molten salts—Data review, Journal of Nuclear Materials, 447 (2014) 271-284.

[35] T. Murakami, T. Koyama, Application of Electrochemical Method to Measure Diffusion Coefficient in Liquid Metal, Journal of The Electrochemical Society, 158 (2011) F147-F153.

[36] J.L. Willit, W.E. Miller, J.E. Battles, Electrorefining of uranium and plutonium — A literature review, Journal of Nuclear Materials, 195 (1992) 229-249.

[37] D.R. Gabe, F. Walsh, The rotating cylinder electrode: a review of development, Journal of applied electrochemistry, 13 (1983) 3-22.

[38] I. Johnson, H.M. Feder, Thermodynamics of the uranium-cadmium system, Transactions of the Metallurgical Society of AIME, 224 (1962) 468.

[39] I. Johnson, M.G. Chasanov, R.M. Yonco, Pu-Cd system: thermodynamics and partial phase diagram, Transactions of the Metallurgical Society of AIME, 233 (1965) 1408.